ISTITUTO NAZIONALE DI FISICA NUCLEARE

Sezione di Milano

INFN/TC-99/04
2 Marzo 1999

STUDY OF THE STABILITY OF THE LHC LOW BETA INNER TRIPLET FOR A NB_3SN DESIGN

Giorgio Ambrosio[1], Francesco Broggi[1], Lucio Rossi[2]

[1)]*INFN-Sezione di Milano,Laboratorio LASA Via Fratelli Cervi 201,I-20090 Segrate, Italy*
[2)]*INFN-Sezione di Milano,Laboratoro LASA, Dip. Scienze Fisiche Università di Milano*

Abstract

The inner triplet of the low β insertion of LHC is made up of four identical NbTi superconducting quadrupoles. To achieve the nominal luminosity of $10^{34}cm^{-2}s^{-1}$ a gradient of 235 T/m is necessary with an aperture of 70 mm. Such a gradient yields a peak field on the coils close to the critical field, endangering the stability for NbTi windings. Improving in the beam and/or collision dynamics depends on the focussing strength of the quads. Nb_3Sn magnet, technologically more complex of the NbTi ones, are a promising solution to improve the gradient beyond the 250 T/m; for this reason we undertook the study of a second generation of low β insertions with Nb_3Sn magnets. Critic for both the construction techniques is the power deposed by the secondary particles generated by the collisions of the 7+7 TeV proton beams. Previous studies estimated the total power released in the NbTi coils to be around 30 W. In this paper different configurations of aperture and gradient of Nb_3Sn coils are examined by tracking the reaction products, as from DTUJET code, in the magnetic field structure and evaluating the energy deposition with the FLUKA code. The stability margin of the magnets is then stated with the analysis of the thermal behaviour with the ANSYS code. The better thermal behaviour using aluminum collars instead of stainless steel is shown. The use of cylindrical absorbers under the magnet leads to an unexpected increase of the peak and of the total power in the second quad of about 50% and of 20% respectively. The operating conditions of all the configurations guarantee a safety margin of operation with no need of any kind of absorbers. In the reference case the maximum power and the peak power deposed in the second quadrupole is 22.4 W and 7.2 mW/cm^3 respectively. The study shows Nb_3Sn seems a viable solution for the low β insertion for LHC if gradient in excess of 250 T/m will be required.

PACS.: 85.25.L

Published by ***SIS–Pubblicazioni***
Laboratori Nazionali di Frascati

1 INTRODUCTION

In the Large Hadron Collider (LHC) the 7 TeV proton beams are focussed at each side of the Interaction Point (IP) by a set of four quadrupoles (Q1,Q2a,Q2b and Q3), series connected, forming the inner triplet (triplet by considering that the two quadrupoles in the middle as a long one). These quadrupoles, 5.5 m long, have a single aperture of 70 mm and a design gradient of 235 T/m[1].

There are currently three design of the interaction region quadrupoles, all employing NbTi conductor and all operating at 1.8 K.

The CERN[2] quad, designed to reach a short sample gradient of 268 T/m, is a four-layer graded-shell coil with stainless steel collars and aluminum spacers for assembly and cool-down control.

CERN has designed and built, in collaboration with Oxford Instruments (GB)[3], three full section 1.3 m long models of a novel design quadrupole; the third of this series has been succesfully tested reaching short sample limit Imax exceeding 250 T/m after training. This quadrupole makes use of very high performance NbTi cable with all kapton insulation.

The KEK[4] quad, a four layer coil with stainless steel collars and interlocking iron yokes, has reached a gradient of 240 T/m in a 1 m long model at 1.9 K[5].

Differing from these two designs, FNAL[6] has designed quad with two layer coil geometry with wide cable and thick stainless steel collars whose nominal short sample gradient is 250 T/m.

The first three 1.3 m long model quads have shown premature quench, below the operating current, exceeding about 230 T/m after initial training.

At 1.8 K and 10 T the superconductor current density in the CERN, KEK and FNAL design have reached 1740 A/mm^2, 1550 A/mm^2 and 1550 A/mm^2 respectively.

The use of highly efficient designs and reduced operating temperatures shows the frontier of operation for NbTi conductor. Increase in the gradient (above 300 T/m) will be possible by using Nb_3Sn instead if NbTi, having Nb_3Sn much higher J_c than NbTi for magnetic field beyond 10 T, as can be seen in Fig.1 where the load line for a 300 T/m gradient quadrupole with an aperture of 70 mm is plotted together with the overall critical current density both for the Nb_3Sn winding at 4.2 and 1.8 K and for the NbTi of the CERN - Oxford quadrupole only at 1.8 K.

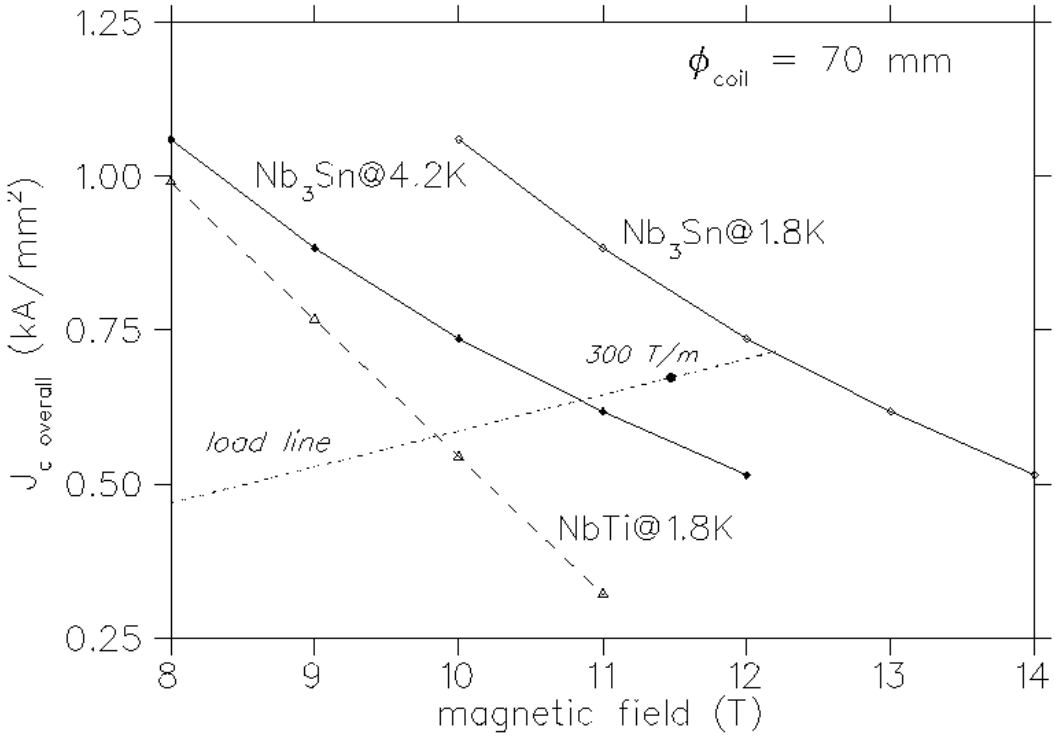

FIG. 1: Critical current density for Nb_3Sn,for NbTi, and 300 T/m in 70 mm aperture load line.

It is clear that a gain in term of focus strength of the triplet can increase the machine performance or relax some critical parameters. For example by lowering the length of the magnets and increasing the gradient, the maxima of the β function, shown in Fig.2 taken from[1)], can be reduced, easeing the beam dynamics.

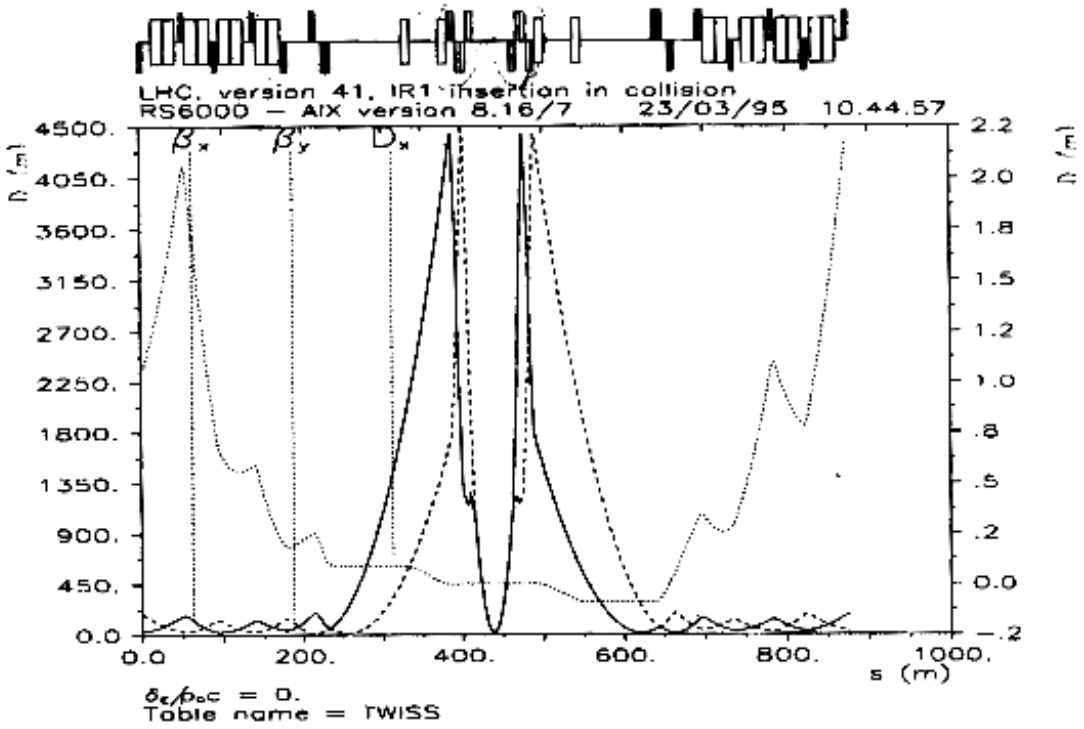

FIG. 2: Collision optics of the high luminosity insertion of LHC.

An increase in the focussing gradient in the same length of the magnets can enhance the luminosity.

Conversely an increase of the aperture provides a better field quality in the beam region with benefical effect on the beam dynamic at the injection.

The use of Nb_3Sn in high field dipoles has been succesfully demonstrated in the tests of two dipole magnets[7),8)], so the applications of Nb_3Sn technology to the quadrupole magnets is straightforward.

To break the barrier of 250 T/m in 70 mm coil aperture we have designed a quadrupole, based on Nb_3Sn conductor, whose schematic cross section is reported in Fig.3.

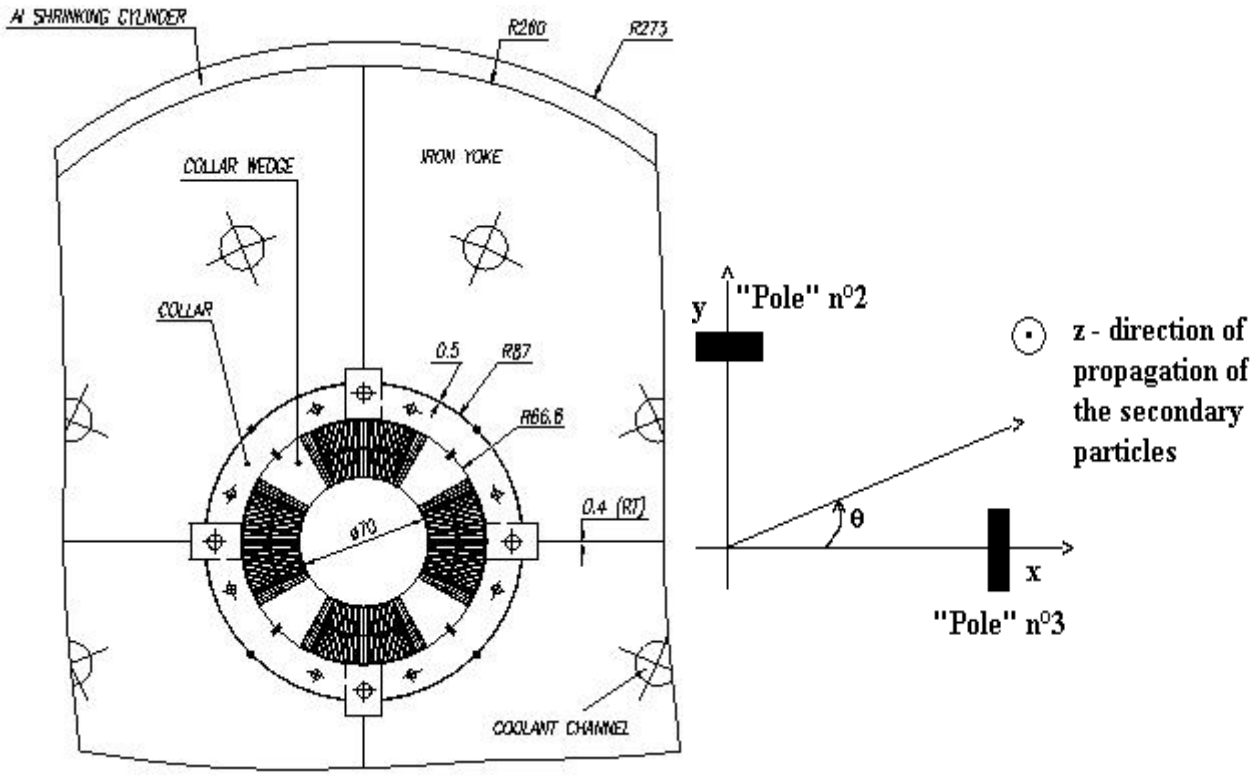

(a) (b)

FIG. 3: (a) Cross section of the Nb_3Sn quadrupole and (b) the pole/shells identification conventions (see text for details).

Nb_3Sn has very high performance in term of critical current (I_c) characteristics versus the magnetic field, but suffers of serious drawback, namely the necessity of high temperature reaction (650 °C or more) and a brittleness that makes coil handling hazardous.

Both the technological solutions, NbTi and Nb_3Sn must take in account the radiation environment, caused by the reaction products of the p-p events.

As a matter of fact the almost 900 W generated by the collision are spread in the insertion, and the magnets must have a large temperature margin in order to withstand this deposition of energy, avoiding a radiation-induced quench. Therefore the choice of the material for the construction of the magnet must take in account the thermal behaviour of the coil, in addition to the mechanical properties.

For this reason we think that an analysis of the power deposed by radiation in the magnets is important but the thermal analysis of the behaviour of the magnet is important too, in order to assess the stability of a magnet in a complete way.

Previous analysis of the power deposed in the low β have been carried out at CERN with a simplified model[9], finding a deposition of about 30 W per magnet.

In this paper the model has been refined in order to have more significant results and to evaluate the local effects of the energy deposition, strongly peaked in the coils mid-planes.

This study starts from a reference case for which the gradient of the main quadrupoles and of the trim quadrupole is 235 T/m and 82 T/m respectively, with an aperture of the main quadrupole of 70 mm, then, in order to evaluate the effects of the gradient and of the aperture, the cases with main gradient of 300 T/m for 70 mm aperture and 235 T/m with aperture of 85 mm have been investigated. The effect of cylindrical absorbers both with uniform thickness and with different thickness in the various magnets (suited absorber case) has been evaluated.

As previously mentioned all the data of the power deposition calculation were used to perform a finite element thermal analysis, done with the ANSYS code, in order to asses the stability margin of the magnets.

In section 2, in its subsections and in section 6 (appendix I) the hypotheses and assumptions don to carry out the calculation are described, while the results of each step are reported in section 3 its subsections and in the sections 7 and 8 (appendixes II and III).

2 DEVELOPMENT OF THE STUDY AND HYPOTHESES

The study has been developed in following four steps:

1. The generation of the secondary particles from 7+7 TeV p-p interaction.
2. The tracking of the secondary particles along the insertion.
3. The evaluation of the deposition of the energy in the quadrupoles.
4. The determination of the stability margin of the magnets, as following from the thermal behaviour by means of 2D/3D finite elements analysis with ANSYS code.

2.1 DTUJET event generator

The generation of the 7+7 TeV proton-proton events occurring at the high luminosity interaction point of LHC are obtained from the DTUJET event generator[10]. In this code the events are generated according to the two component dual parton model which include single diffraction.

The events taken in consideration are the inelastic scattering (where both the two protons transform in a cascate of secondary particles) and the single diffractive. In the single diffractive events one of the two primary protons maintain its own identity while the other transforms into the reaction products.

According to the “Yellow Book”[1] the cross section for the two kind of events are σ_{sd}=12 mbarn and σ_{in}=60 mbarn. However for the evaluation of the power deposed we

consider a total cross section of 80 mbarn because in the code DTUJET for generating the events this is the cross section used.

The elastic scattering has an important cross section (σ_{el}=40 mbarn) but this kind of interaction causes the scattered protons to have a perturbed longitudinal momentum, so they do not hit in the low β insertion but, after many turns, they can be absorbed by the collimators installed in a warm section (betatronic (β-) cleaning and momentum (p-) cleaning).

For our study 1300 events has been generated and by considering only one side of the interaction section, by changing the momentum sign for the particle travelling toward the other part of the section, we can double the statistics.

2.2.1 Coordinate system and identification of the poles

The coordinate system used is a dextrorse xyz system referred to the secondary beam, as shown in Fig. 3b.

In the quadrupole section the sequence of the field is FDDF for the primary 7 TeV proton beam , so, for the secondaries the field sequence is DFFD .

Here for focusing we mean in the horizontal plane for a positive charged beam.

With this configuration the pole axis are at 45°,135°,225° and 315° but , for our convenience when discussing the result we will use the word “pole” to mean the shell of the coil.

With this convention we will identify the pole n°1 at 180°, pole n° 2 at 90°, pole n° 3 at 0° and pole n° 4 at 270° (see Fig.3).

2.2.2 Finite crossing angle

The crossing angle of the beams in LHC is 200 μrad so the output of the event generator must be transformed in a frame whose center of mass transverse velocity is such that the two beam seen from it intersect under an angle of 200 μrad.

2.2.3 Beam line layout

The parameters of the beam line where the particles are tracked is shown in Table 1, while the layout of the beam line is shown in Fig. 4.

TAB. 1: Main parameters of the beam line of the insertion.

ELEMENT NUMBER	**APERTURE RADIUS (mm)**		**LENGTH (m)**	**DESCRIPTION**	**DISTANCE from I.P. (m)**
	Φ=70	**Φ=85**			
1	31.5	31.5	19.0	Detector + free space	19.0
2	15.0	15.0	1.8	Collimator	20.8
3	31.5	31.5	2.2	Free space collimator - Q1	23.0
4	**31.5**	**39.0**	**5.5**	**Q1 quad**	**28.5**
5	31.5	39.0	0.3	Free space Q1 - Q01	28.8
6	31.5	39.0	1.5	Q01 inner triplet trim	30.3
7	31.5	39.0	0.7	Free space Q01 - Q2a	31.0
8	**31.5**	**39.0**	**5.5**	**Q2a quad**	**36.5**
9	31.5	39.0	0.4	Free space Q2a – ITC	36.9
10	31.5	39.0	0.2	ITC	37.1
11	31.5	39.0	0.4	Free space ITC - Q2b	37.5
12	**31.5**	**39.0**	**5.5**	**Q2b quad**	**43.0**
13	31.5	39.0	0.4	Free space Q2b – ITC	43.4
14	31.5	39.0	0.2	Inner triplet corrector	43.6
15	31.5	39.0	1.7	Free space ITC - Q3	45.3
16	**31.5**	**39.0**	**5.5**	**Q3 quad**	**50.8**

In the column labelled as “distance from I.P.” is reported the distance of the end of the element from the interaction point. (ITC is for Internal Triplet Corrector).

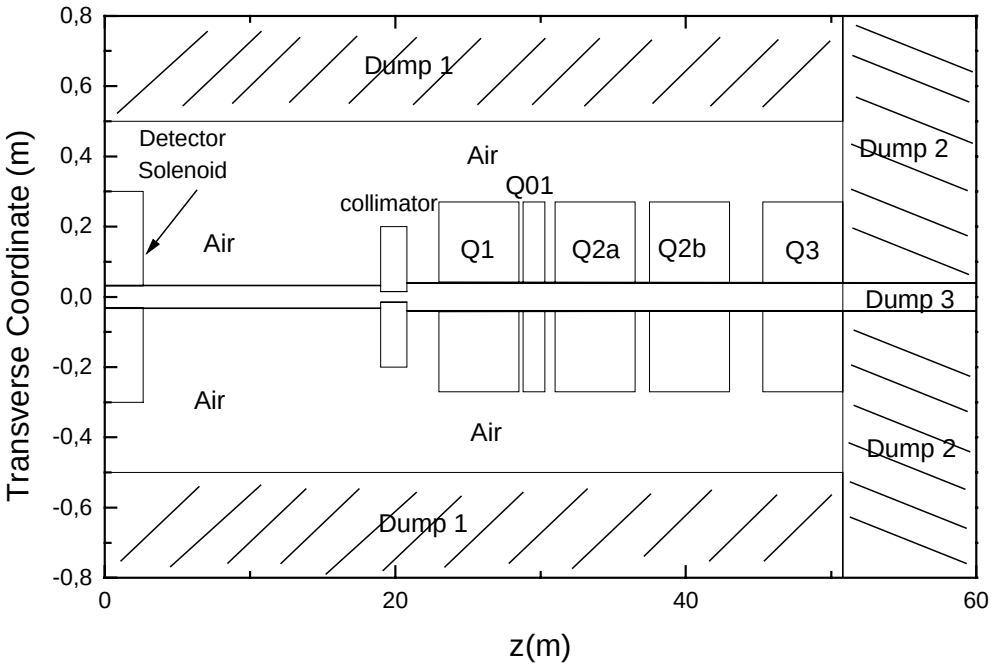

FIG. 4: Schematic view of the longitudinal insertion layout for quadrupole aperture of 85 mm. When the quad aperture is 70 mm the diameter of the beam pipe before and after the collimator is the same as before the collimator (see table 1). The dumps, as indicated in Tab. 3, are shown.

Note that in Fig. 4 the beam pipe after the collimator is larger than that one before the collimator, due to the possibility to accomodate a larger aperture.

In case of 70 mm quadrupole aperture the beam pipe diameter is the same both before and after the collimator as reported in Table 1.

2.2.4 Magnetic field along the insertion

The detector configuration used to track the particles is the ATLAS solenoid [11)] that will be located at the intersection point 1[1)]. The magnetic field used to track the particle is assumed to be generated by a thin and finite solenoid calculated according with the usual analytical formula:

$$B_z(z) = KB_0\left(\frac{\frac{L_s}{2} - z}{R^2 + (\frac{L_s}{2} - z)^2} + \frac{\frac{L_s}{2} + z}{R^2 + (\frac{L_s}{2} + z)^2}\right) \quad (1)$$

for a finite solenoid of radius R = 1.1 m, L_s = 5.3 m length and B0 = 2.0 T peak field.

In Fig. 5 the axial component of the field of the ATLAS solenoid is shown.

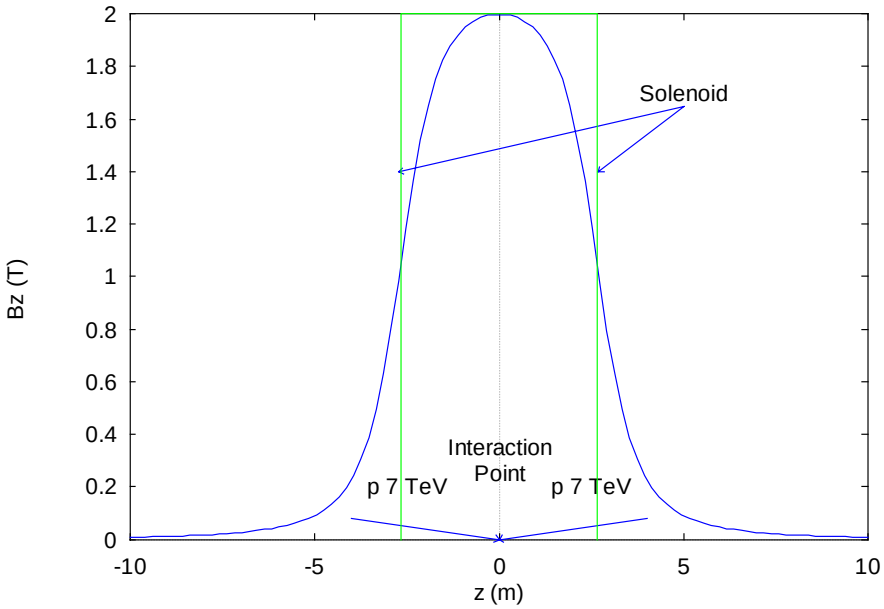

FIG. 5: Axial magnetic field component of the ATLAS solenoid.

The radial component is derived by considering the simmetry of the field having no azimuthal component and from the Maxwell equation divB=0, so, at first order:

$$B_r(z) = -\frac{r}{2}\frac{\partial \mathrm{Bz}}{\partial \mathrm{z}} \quad (2)$$

The field of the quadupoles is assumed to be the nominal one, without z dependence (hard-edge model), so it is :

$$\begin{gathered} \mathrm{Bx} = \mathrm{Gy}\ ;\ \mathrm{By} = \mathrm{Gx}\ ;\ \mathrm{Bz} = 0\ \text{ for the F quad} \\ \mathrm{Bx} = -\mathrm{Gy}\ ;\ \mathrm{By} = -\mathrm{Gx}\ ;\ \mathrm{Bz} = 0\ \text{ for the D quad} \end{gathered} \quad (3)$$

where G is the gradient.

2.3.1 Geometry, magnetic field and cut-offs for FLUKA calculations

FLUKA[12] (FLUctuating Cascade) is a general multi-purpose Monte Carlo program for the simulation of high energy (up to 20 TeV) hadronic and electromagnetic cascade in a 3D, multi-region and multi-medium environment.

The longitudinal geometry is the same as above reported for the tracking.

Beam dumps, to evaluate the forward/backward and lateral escaping power, have been added at z = - 0.5 m at the end of Q3 (z = 50.8 m).

The lateral dump is a cylinder of inner radius of 0.5 m.

The quadrupole geometry has been defined precisely as possible both in its geometrical shape and in its material composition.

A cross section of the beam line and of a quadrupole is shown in Fig.3 and in the figures of section 6 (appendix I).

The energy deposed in the insertion elements is stored both in an integral mode i.e. region by region, and in small bins, in order to get the local energy distribution and insulate the peak of power deposition.

The transverse binning geometry used are shown in section 6.

The reference longitudinal length of the bin was 50 cm; in addition, for the case 70-235-82, the length of 10 cm on the hottest quadrupole was used too, in order to see the longitudinal dependence of the power deposition.

The cut-off values are 1 MeV for the hadrons, 1.5 MeV for the electrons and positrons, 0.2 MeV for the photons and 0.4 eV for the neutrons.

The magnetic field in the quadrupole coils, collar, yoke etc. is calculated by POISSON[13].

2.4.1 2D Finite elements thermal analysis

The heat deposition data were input in a 2-D FE model for a steady state, linear thermal analysis by means of the ANSYS code. We have evaluated analytically that heat conduction in longitudinal direction gives a contribution of few percent to the power dissipation in the hot spot.

Therefore we think that a 2-D model, using the power density released in the hottest longitudinal section (the first 0.5 m of Q2a) instead of the average power density, is a good, slightly conservative, approximation.

The quadrupole cross section was described in details, with the following regions (starting from inner radius): 0.35 mm ground insulation, inner layer, 0.7 mm layer to layer insulation, outer layer, 0.7 mm ground insulation and 20 mm thick collars made of stainless steel or aluminum alloy. At the top of the two shells there is the pole wedge made of stainless steel.

The thermal conductivity of the coil package has been computed with a simple conservative model representing the coil as a pile of alternating cables and cable to cable

insulation. In the cables the heat is supposed to flow only longitudinally along the pure copper of each strand (i.e. no thermal conduction between adjacent strand is considered). The cable conductivity is therefore depending on the cabling angle and the transposition pitch. The insulation is supposed to be made of G10 with non-isotropic properties.

Heat exchange to helium occurs through the surface of the inner bore and through the outer surface of the collars. For the heat transfer coefficient a conservative value of 1000 W/m2K at 1.9 K has been used.

In the coil, the insulating regions and the pole wedge the power has been distributed according to the results of FLUKA, in the collars the total power was concentrated in few elements near the mid-plane (an example can be seen in Figure 6).

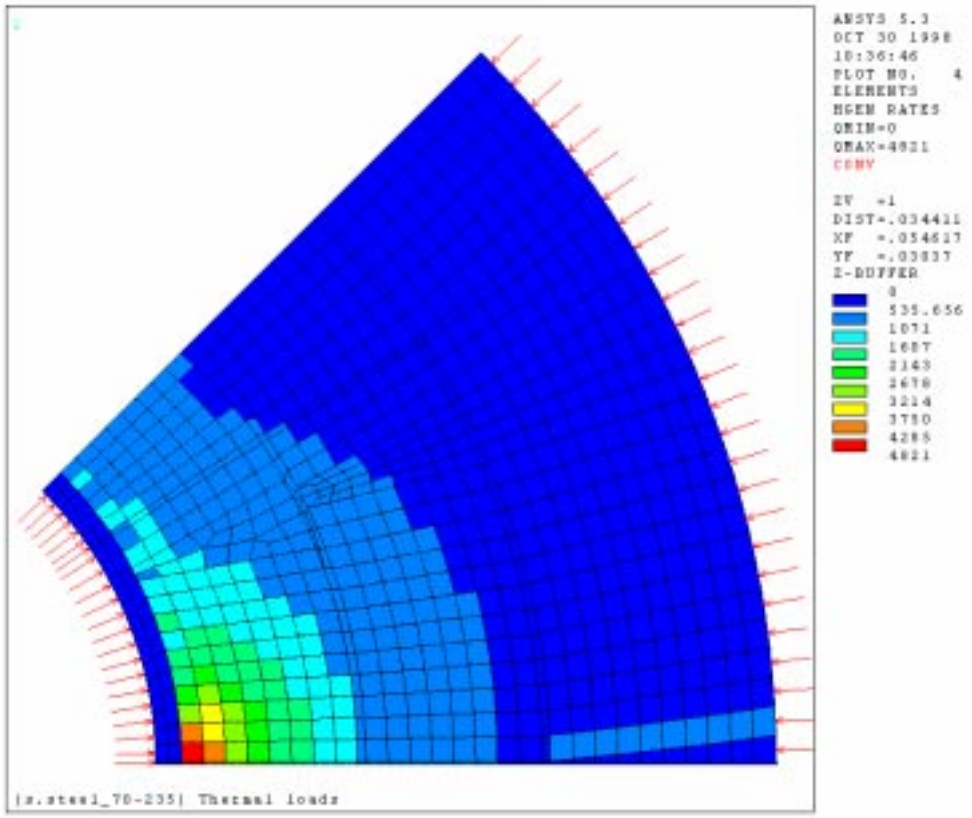

FIG. 6: Thermal loads (i.e. power density (W/m^3) of the source of the heat) for the ANSYS calculations in the reference case.

3 RESULTS

As told in the introduction this section reports the results of the calculations described in subsections like done for the discussion of the hypotheses. Details are reported in sections 7 and 8 (appendixes II and III).

3.1 Generation of the events by DTUJET code and particles treated

The particles generated in the collisions and their total energy are shown in the Table of section 7 with figures showing the proton distribution of the momentum, energy and magnetic rigidity.

The energy corresponds to a beam power of about 900 W, at the nominal maximum luminosity for a single experiment of $1x10^{34}$ $cm^{-2}s^{-1}$. As a matter of fact the power carried by the reaction product is the 18.2 x 10^6 GeV realized by the two beams in 1300 interactions so:

$$P = \frac{18.2x10^6 \text{ x } 10^9 \text{ x } 1.602x10^{-19} \text{ x } 10^{34} \text{ x } 80 \text{ x } 10^{-27}}{1300} = 1794.2 \ W \qquad (4)$$

so the power realized by a single proton beam is:

$$P_{beam} = \frac{P}{2} = 897 W \qquad (5)$$

As can be seen in section 7, most of the energy is carried by protons, pions and neutron respectively. The charmed particle contribution is very small so they are neglected and not treated neither in the tracking nor in FLUKA.

The secondary charged particles are then tracked in the magnetic structure of the insertion by our analytical code. When the charged particles hit the beam pipe are processed by FLUKA. The neutral particles are directly passed to FLUKA at the generation

3.2 Tracking of the particles in the insertion

The results of the tracking of the DTUJET products along the insertion are reported in the Table of section 8. The data refers to the reference case of 70 mm aperture, 235 T/m for the gradient of the main quadrupoles and 82 T/m for the gradient of the trim quad.

In Fig. 7, 8 the trajectories in the horizontal and vertical plane of the first 10 protons are shown respectively. Fig. 9 show the radial coordinate along the insertion. In the pictures the trajectories of the same protons as from a head on collision is shown too.

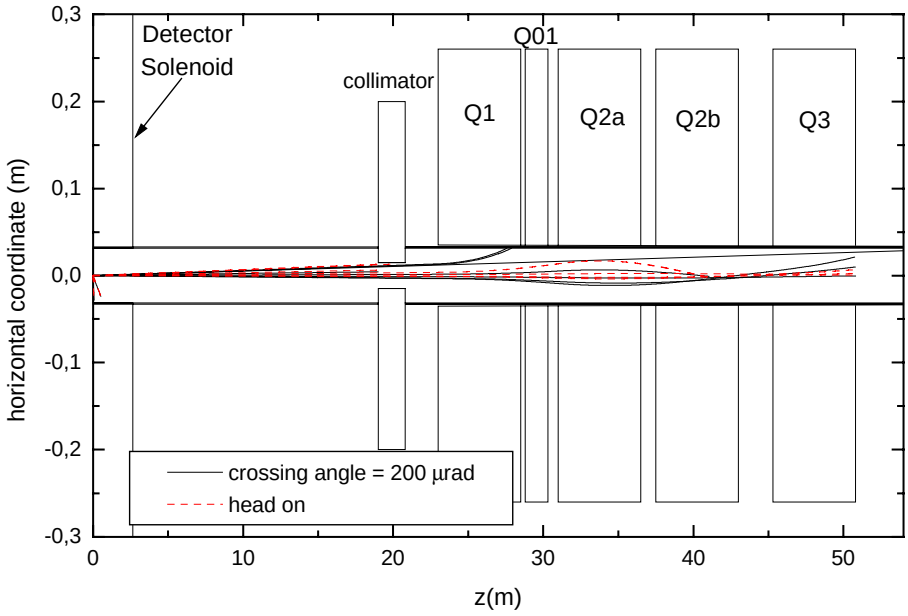

FIG. 7: Trajectories of 10 protons in the horizontal plane, for a “head on” collision and for collision with crossing angle of 200 µrad.

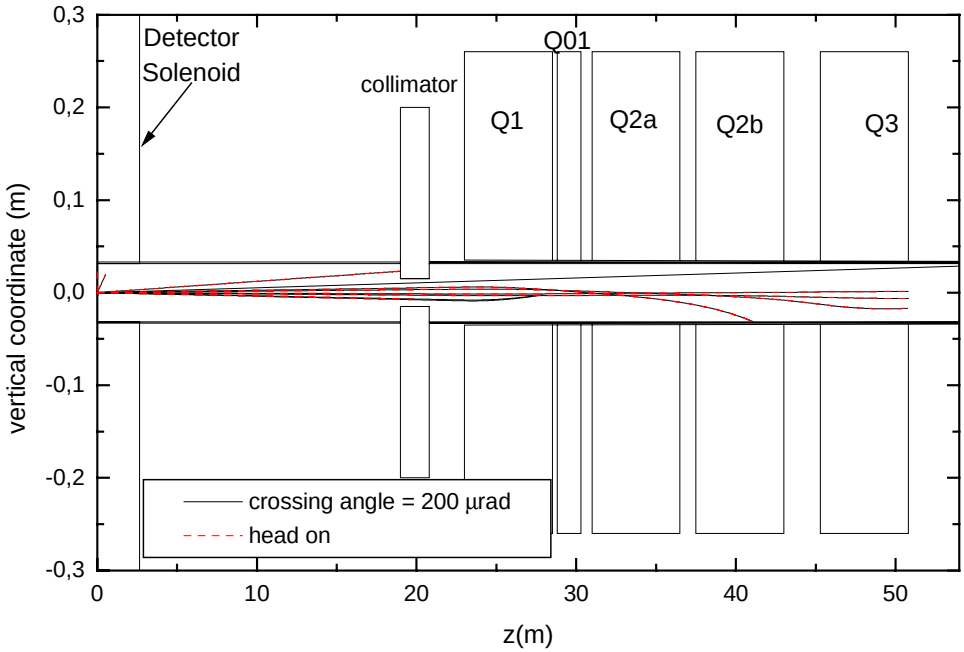

FIG. 8: Trajectories of 10 protons in the vertical plane, for a “head on” collision and for collision with crossing angle of 200 µrad. In this plane there is no effect of the crossing angle on the trajectories.

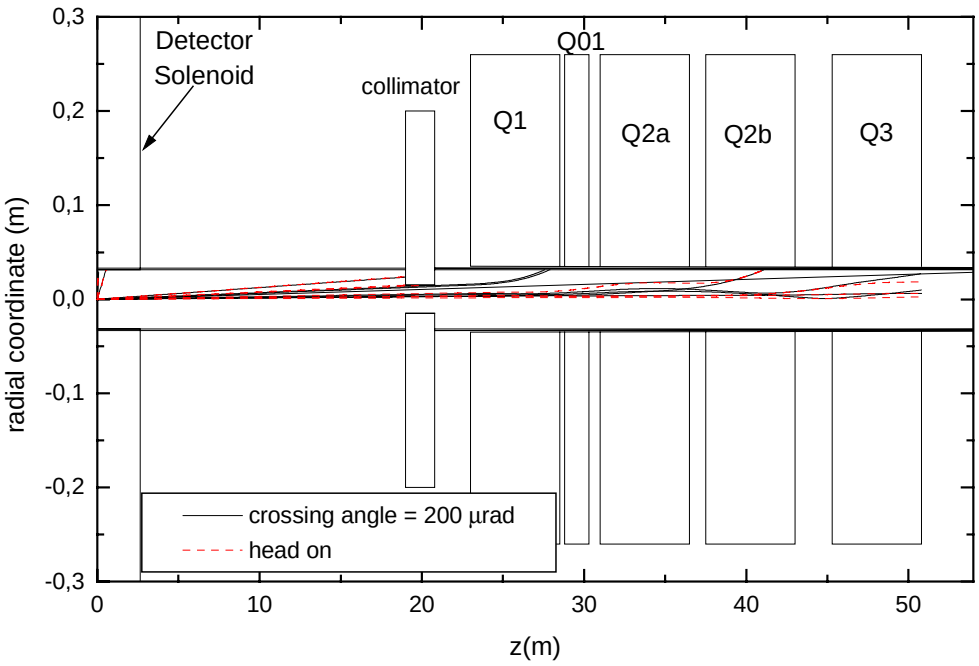

FIG. 9: Radius of the trajectories of 10 protons for a “head on” collision and for collision with crossing angle of 200 µrad.

The trajectories in the vertical plane for the head on collision and for the crossed beams are obviously the same.

The charged particles decaying in flight during the tracking are neglected, but this does not affect the calculation because the fraction of energy not computed by neglecting the dacaying is negligible. As a matter of fact the energy neglected in the tracking is about $3.35\ 10^4$ GeV ($2.0\ 10^4$ GeV of the charmed particles and $1.35\ 10^4$ GeV of the decaying in flight), but this is less than 0.2% of the total energy treated.

The FLUKA code conversely take into account the decaying of the particles and handle treats the decay products for the computation of the energy deposed.

3.3 FLUKA runs

The results of the FLUKA runs are reported in the following subsections. At first the reference case is analyzed, then all the other cases are compared to the reference one.

3.3.1 The reference case 70-235-82

The total power treated by FLUKA, in the reference case of 235 T/m main quadrupole gradient, 82 T/m for the trim quad and aperture of the magnets of 70 mm, is about 690 Watts shared as in the Table 2.

TAB. 2: Power sharing as from FLUKA elaborations

Detailed POWER description of FLUKA elaboration	**(W)**	**(W)**
Deposed by ionisation	98.2	633.9
Deposed by e m cascade	513.3	
Deposed by nuclear Recoil and heavy ions frag.	3.2	
Deposed by particle below threshold	19.1	
Deposed by low energy neutrons	<0.1	
Escaping the system	<0.1*	
Discarded	5.5	
Internal nuclear reactions	51.7	
TOTAL Power treated by FLUKA	**690.6**	
Power of charged particles in the forward dump as from tracking	**205.8**	
Power carried by charmed particles	1.0	
Power carried by charged particles decaying in flight	0.7	
TOTAL POWER	**898.1**	

(*) This is the power escaping the dumps. The dumps take into account both the power in the forward direction and the power laterally radiated after having crossed the magnet structure.

The power discarded is the power computed by FLUKA only for the total balance, but it is not tracked. It is mostly due to the neutrinos.

The power of the charmed particles is not treated, neither by the tracking nor by the FLUKA code, as well as the power of the charged particle decaying during the tracking, i.e. decaying in flight. This does not affect the calculation, as already explained in section 3.2.

In the Table 3 the distribution of the 633.9 W deposed, as from the region energy deposition evaluated by FLUKA, is shown.

TAB. 3: Power deposition in the various elements. See Fig. 4 for the identification of the dumps

ELEMENT	**Power (W)**
Beam pipe before the collimator	20
Collimator	140
Q1	11.5
Q01	8.7
Q2a	22.4
Q2b	7.5
Q3	17.4
Beam pipe after the collimator	14.0
Power laterally escaped (Dump 1)	131.5
Power laterally forward escaped (Dump 2)	37.7
Power forward escaped (Dump 3)	223.2
Total	**633.9**

The statistical error, as from different runs with independent random seeds, is about 1% for the region binning, 3% for the medium binning, 4% for the small binning and 7% for the very small binning.

As we can see from Table 3 the “hottest” quadrupole is Q2a, the second one, and the maximum peak power in it is in the first part, respect to the I.P. In Table 4 the values of the peak power density are shown for the various binning geometry used (see section 6 for details of the binning).

TAB. 4: Power density for the different binning geometry

	Binning 1 (medium) (V =12.17 cm^3)	Binning 2 (fine) (V =2.93 cm^3)	Binning 3 (very fine) (Vol. =0.6 cm^3)
Power Density (mW/cm^3)	3.2	5.2	7

Other consideration on the reference case will be done in the following sections, where the comparison with the other cases will be carried out.

3.3.2 Other cases

The cases studied are listed in Table 5 following table (the first line is the reference case).

TAB. 5: The cases studied. In the “suited absorber” case the absorbers thickness refers to the absorbers under Q1,Q01,Q2a,Q2b,Q3, respectively.

Case Number	Aperture (mm)	Main Gradient (T/m)	Trim Gradient (T/m)	Absorbers Type / Thickness (mm)
1	70	235	82	No
2	70	235	82	Cylindrical uniform / 5
3	70	300	105	No
4	85	235	82	No
5	70	227	80	Suited / 12; 10; 4.5; 4.5; 4.5

The cases with the “suited absorbers” refers to the case in which the absorber thickness is not constant under the quadrupoles; the values reported are the thickness of the absorbers under Q1,Q01,Q2a,Q2b and Q3 respectively. In this case the main and the trim gradient are not the same than the reference case, because this is a very conservative case, in which the aperture of the collimator is reduced to 14 mm too. Nevertheless we think that the results can be compared as well because in this case the trajectories of the particles in the material are quite similar, the variation of the energy deposition is less than the statistical accuracy of the calculation.

As a matter of fact the main difference should be if the magnetic field would not be taken into account; in this cases the trajectories of the particles would be straight lines (neglecting the scattering by the atom of the material) instead of spirals, leading to a energy deposition more diffused.

In Table 6 the data of the integral (region by region) power deposition are shown.

TAB. 6: Integral (region by region) power deposition for the various cases.

ELEMENT	**Power (W)**				
Cases	**1**	**2**	**3**	**4**	**5**
Beam pipe before the	20	19.7	19.8	19.7	19.7
Collimator	140	135	137	136	149
Q1 / Absorber	11.5	12.1 / 5.6	14.4	10.6	13.3 / 12.2
Q01 / Absorber	8.7	6.5 / 5.0	11.0	8.2	4.5 / 4.3
Q2a / Absorber	22.4	27.5 / 11.0	25.3	19.4	10.8 / 4.9
Q2b / Absorber	7.5	10.3 / 8.5	9.5	8.0	7.8 / 5.3
Q3 / Absorber	17.4	14.5 / 11.0	20.4	6.3	14.6 / 10.6
Beam pipe after the coll.	14.0	9.5	17.0	9.8	5.6
Laterally radiated (Dump 1)	131.5	135.0	132.5	130.0	135.0
Laterally forw. Radiated (Dump 2)	37.7	32.1	40.2	37.9	32.6
Forward radiated (Dump 3)	223.2	211.1	229.5	241.8	210.5
Total	**633.9**	**654.4**	**656.6**	**627.7**	**640.7**
Power of charged particles in the forward dump as from tracking	205.8	180.4	177.6	208.4	202.9
Total	**839.7**	**834.8**	**834.2**	**836.1**	**843.6**

In Fig. 10 the data of the power in the quadrupoles and in the absorbers, when present, are visualized.

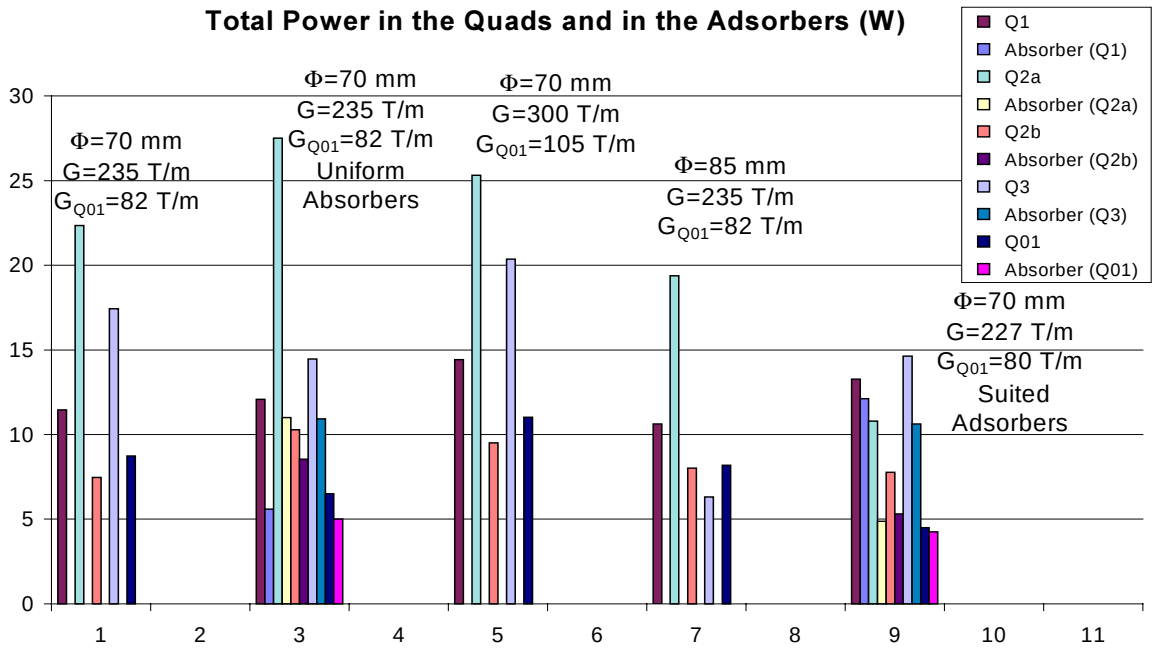

FIG. 10: Power in the quadrupoles and in the absorbers (when present), for the various cases.

As we can see in table 6 and in its graphical representation of Fig.10 the “hottest” quadrupole is the second one, Q2a, with exception of the case with the suited absorbers.

In Fig. 11 the power deposed in the first shell, i.e. the inner one, of Q2a is shown. The asymmetry between the poles 1 and 3, i.e. the horizontal ones, is due to the crossing angle of the primary proton beams.

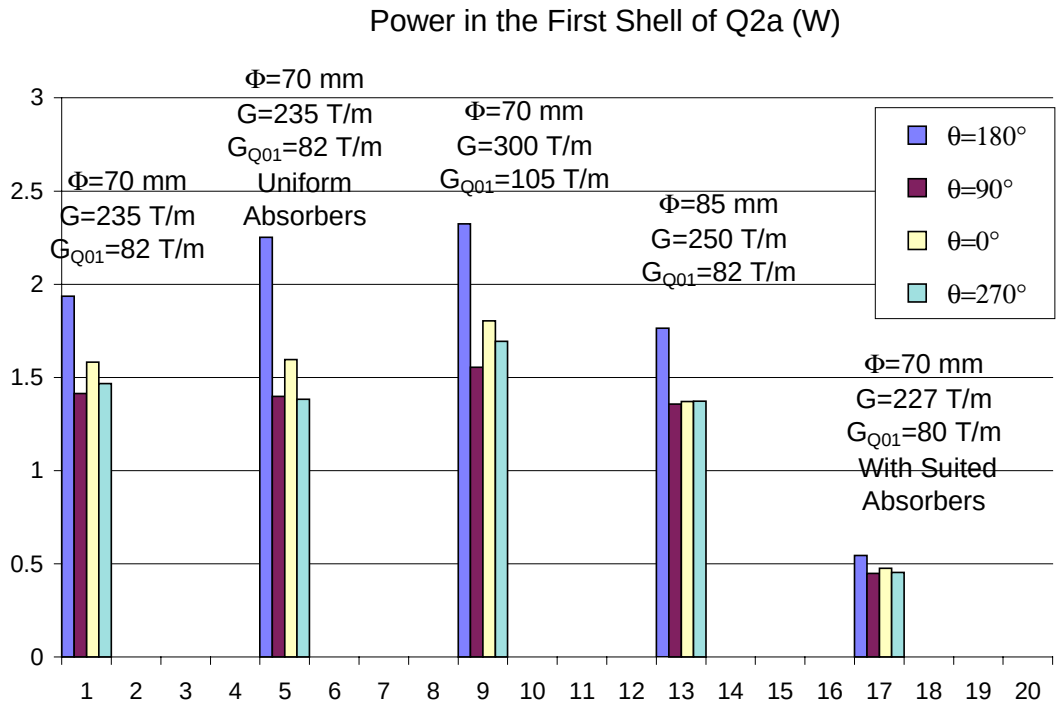

FIG. 11: Power in the inner shell of the second quadrupole. The asymmetry between the horizontal poles is due to the crossing angle, in the horizontal plane, of the primary beams.

From the data above we can even see that the using of the cylindrical absorbers with uniform thickness under the magnets increase the power deposed, in opposition with one can think.

The reason of this behaviour can be due to the fact that the smaller aperture of the absorbers does start the cascade of particles that would travel longer deposing their energy elsewhere in the last quadrupoles where there are not critical conditions or even escaping forward, outside the triplet. So the use of the absorbers must be carefully evaluated and their dimensions suited for the particular case, as shown by the results of the cases with the suited absorbers.

In Table 7 the maximum peak power density in Q2a is shown for the different binning geometry in the various cases studied

TABLE 7 - Peak power density in the inner shell of Q2a for the cases studied (see table 5 for identification of the cases). See section 6 for details on the binning geometry.

	Volume of the bins for Φ = 70 mm / 85 mm (cm^3)		
	12.2 / 12.5	**2.9 / 3.125**	**0.6**
Case	**Power density (mW/cm^3)**		
70-235-82	3.2	5.1	7.2
70-235-82 Uniform Absorbers	5.7	8.2	9.8
70-300-105	4.1	7.5	--
85-235-82	3.8	5.0	--
70-227-80 Suited Absorbers	--	0.3	0.7

The maximum of power deposition for Q2a is in the horizontal plane, with the exception of the suited absorbers case where it is about 23 ° above the horizontal plane. For the other quadrupoles the maxima vary azimuthally, because of the different focusing properties of the magnets and of the particle dynamics.

In Fig. 12 the maximum power density in the inner shell is plotted versus the longitudinal coordinate, independently on the radius and the azimuthal angle at which it occurs, as from the “medium” binning.

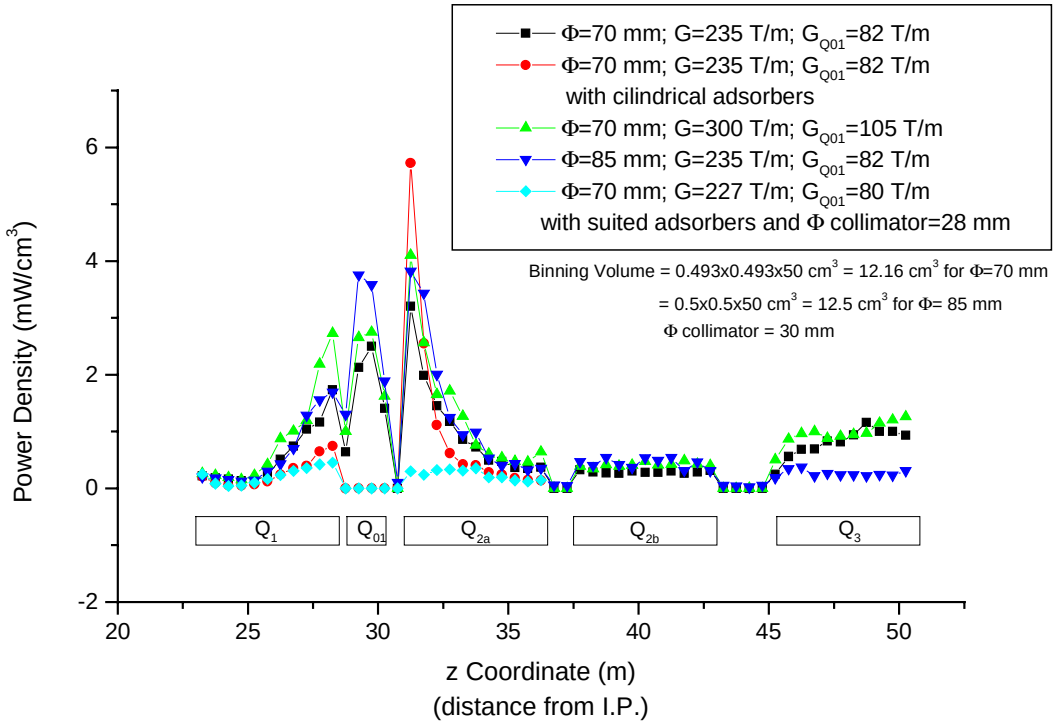

FIG. 12: Maximum power in the inner shell for the whole triplet. It is the maximum in the shell as from the "medium" binning, wherever azimuthally or radially it occurs.

In Fig. 13 the maximum power density deposed in the inner shell of Q2a is shown for the different cases and for the smaller binning geometries.

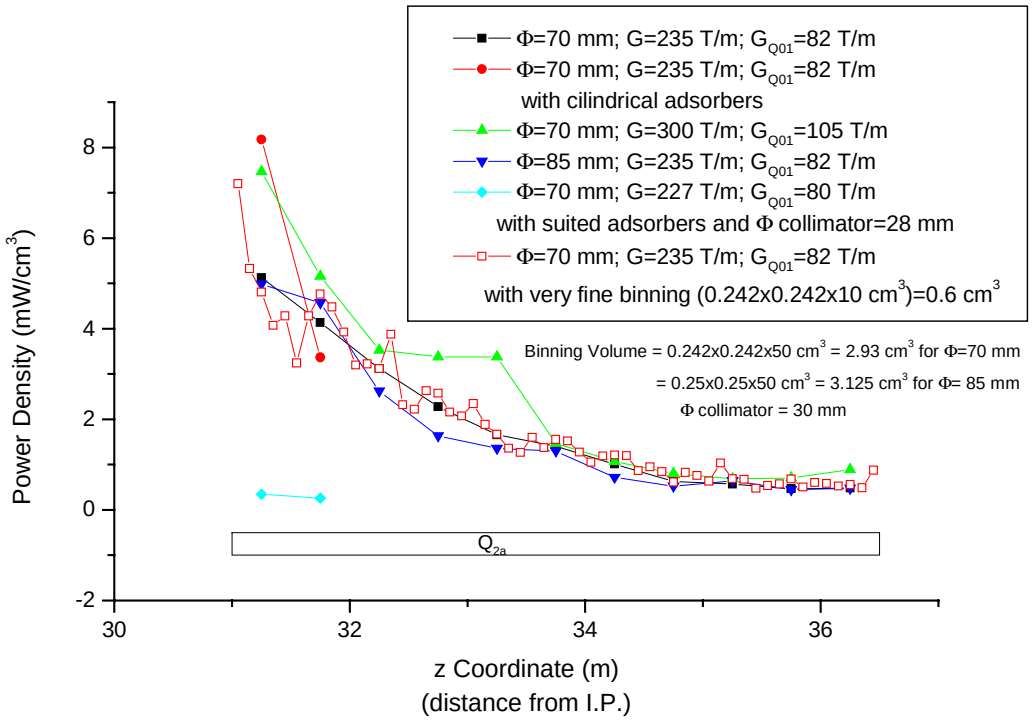

FIG. 13: Maximum power in the inner shell for the second quadrupole (Q2a) in the various cases for the smaller binning geometries.

As we can see from Fig.13 the longitudinal refining of the binning done in the reference case (with 10 cm long bins), plotted with open square, does not provide a refinement in the evaluation of the power deposed respect to what given with 50 cm binning length, plotted with the filled square.

Fig. 14 shows the azimuthal power density distribution along the insertion obtained with the “medium” binning (see section 6).

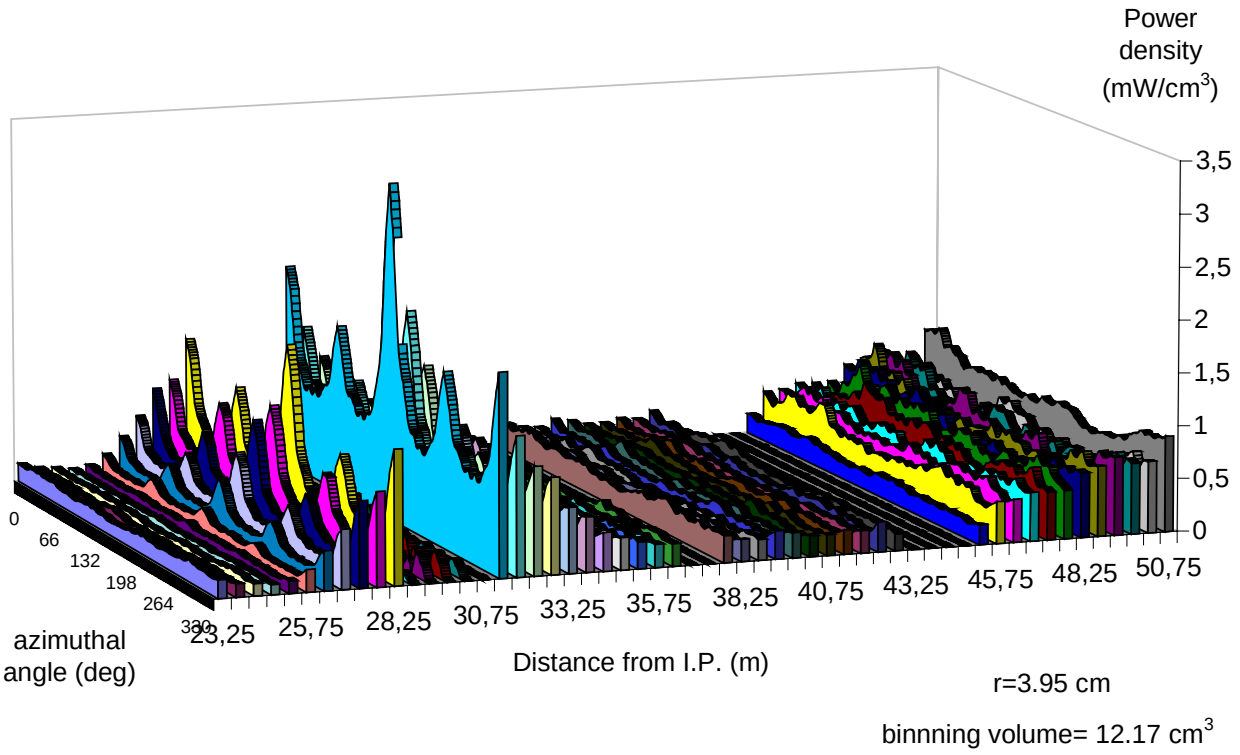

FIG. 14: Angular power distribution in the inner shell of the insertion for r=3.95 cm for the reference case for the “medium” (see section 6) binning geometry.

At different radii the power distribution shows the same behaviour but lower intensity.

Let’s consider now the azimuthal distribution of the power when the absorbers are placed under the magnets. As already seen for the integral (region by region) power deposition, the use of uniform absorbers leads to an increase of the power deposed in the main quadrupoles, with the exception of Q3. The same effect is present for the peak power distribution as can be seen in Fig.15 -17.

Figs. 15 and 16, similarly to Fig.14 show the power distribution in Q1 and Q2a for the two case considered of absorbers, i.e. the uniform absorber case and the suited absorber case.(in these figures the trim quadrupoles Q01 is neglected).

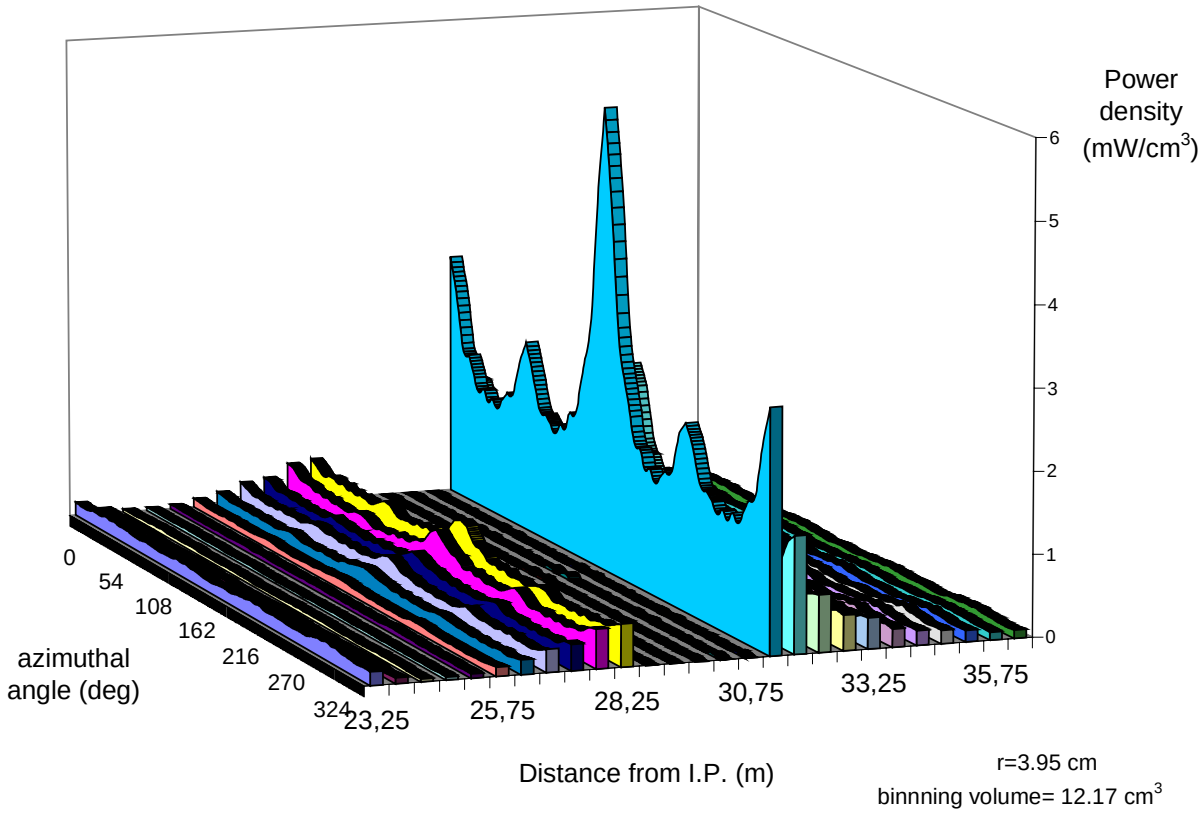

FIG. 15: Angular power distribution in the inner shell of Q1 and Q2a for r=3.95 cm for the “medium” (see section 6) binning geometry, when uniform cylindrical absorbers are under the quadrupoles.

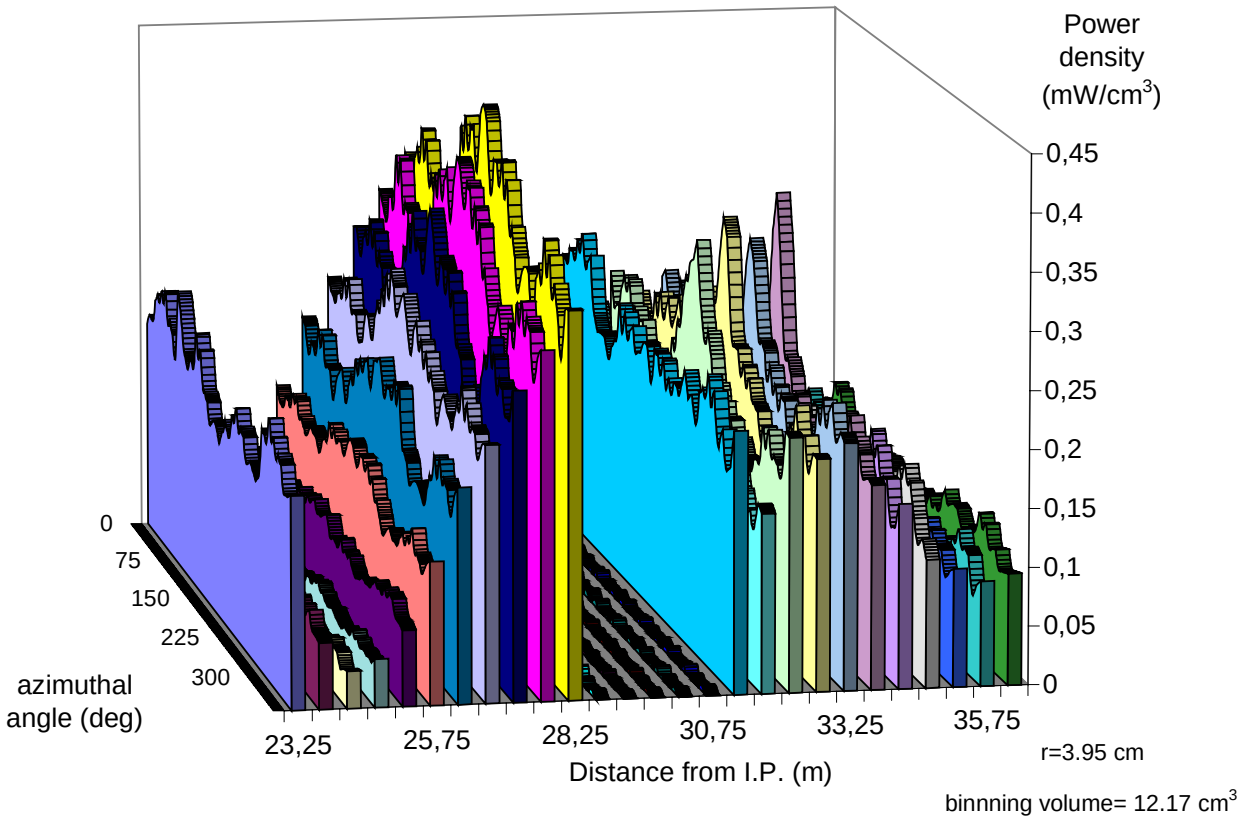

FIG. 16: Angular power distribution in the inner shell of Q1 and Q2a for r=3.95 cm for the “medium” (see section 6) binning geometry, in the “suited adsorber case”.

In Fig.17 the azimuthal distribution of the power density at radius of 3.63 cm, i.e. where the maximum in the inner shell occurs, in the first part of Q2a is shown.

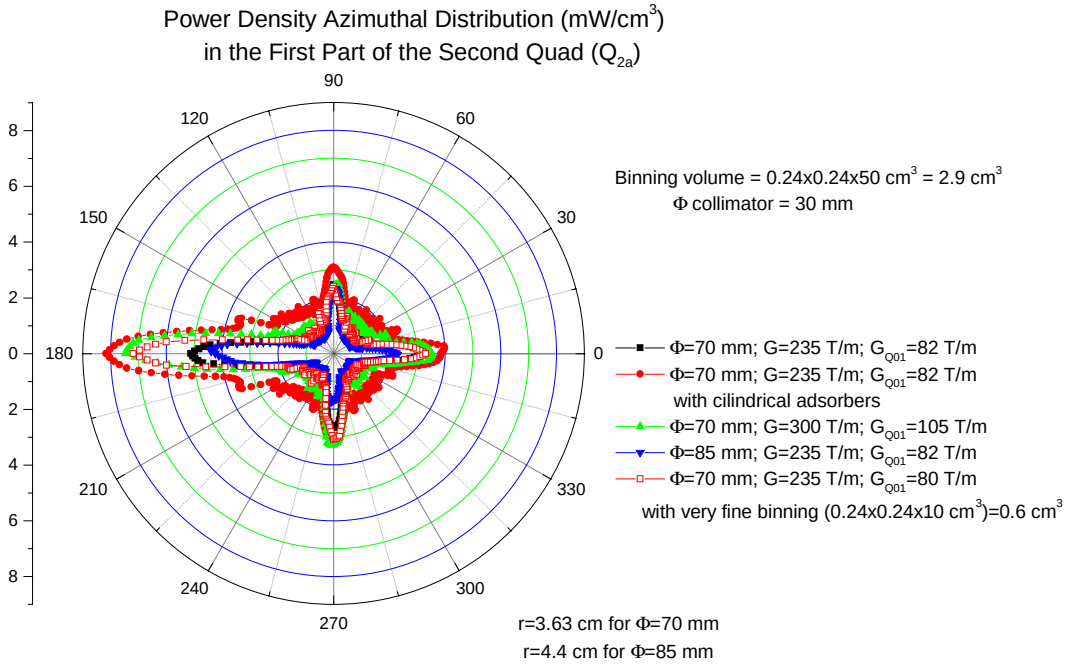

FIG. 17: Angular power distribution in the inner shell for Q2a for r=3.63 cm in the various cases and for the smaller binning geometries. The cases with the suited absorbers is not shown being the power too low to represented on this scale (see Fig.16).

In Fig.18 the angular power density distribution in the first part of Q2a at radius of 3.63 cm is shown for the case of the suited absorbers, for the fine binning, to show how in this case the power distribution is very uniform, without the peak of the cases without the absorbers.

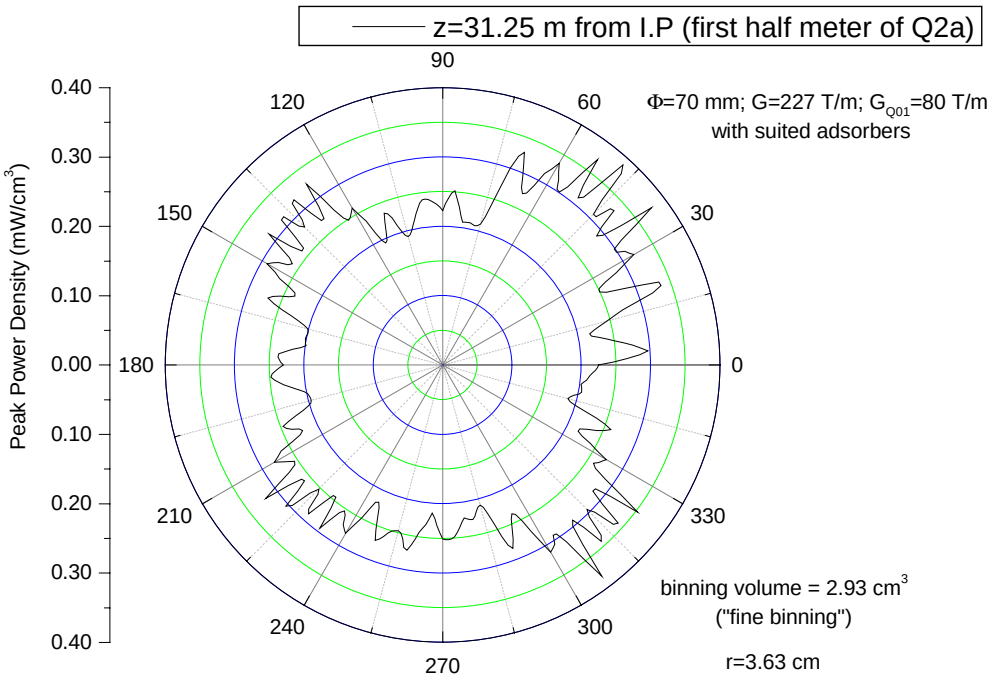

FIG. 18: Angular power distribution in the inner shell in the first part of Q2a for r=3.63 cm for the “fine” binning geometry, in the “suited absorber case”.

3.3.1 Observations and commets on the FLUKA runs

The results of the FLUKA runs reported in the previous section show that in the reference case the total power and the peak power released in the coils of the quadrupoles is “not high” or critical (the meaning of “not high” will be clear after the thermal analysis, done in the following sections).

At this point we can only use a sort of “rule of thumb”, experimentally determined[14)], by which the critical value of the power deposition for a NbTi (and we can roughly assimilate the Nb_3Sn) magnets is 14 mW/cm^3.

From the results of the previous sections the power deposed in the quadrupoles is always lower than this value so we can optimistically state, so far, that all the configurations considered are safe.

Here we can outline the fact that the increasing in the gradient increases the power deposition, with respect to the reference case, while enlarging the aperture leads to a reduction of the power deposed in the magnets (especially Q2 and Q3) relaxing the operating conditions, with a larger safety margin for the quadrupoles.

The use of absorbers must be carefully evaluated and the thickness of the absorbers must be well dimensioned, probably considering the reducing of the aperture of the collimator because, as shown, it can produce the opposite effect of increase the power deposition in the magnets, instead of reducing it.

In the following section the thermal behaviour of the magnets will be examined, in order to evaluate the stability limits of the magnets. This will be done by using the data of the power deposed as from FLUKA calculations as heat source in the structure of the magnet.

We will see that the “rule of thumb” of the 14 mW/cm^3 of peak power limit is fulfilled.

4 THERMAL ANALYSIS

The results of the thermal analysis in case of the hottest section for the reference case (70-235-82) with stainless steel collars in He bath at 1.9 K are reported in Figures from 19 to 22.

The temperature distribution in the whole section and in the coils is shown in Figures 19 and 20.

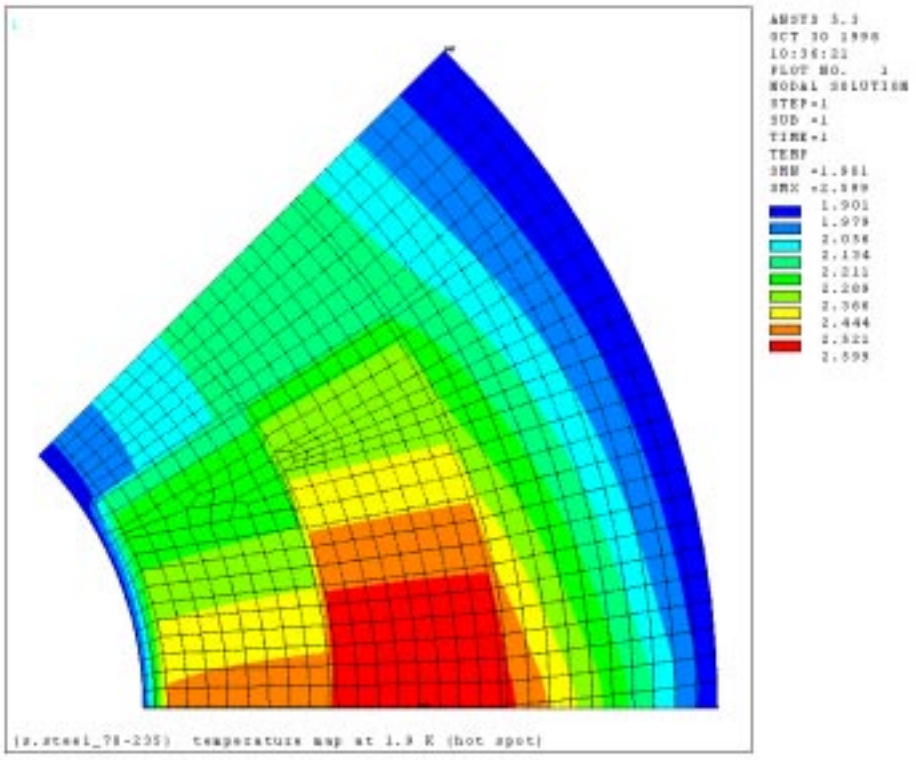

FIG. 19: Temperature distribution for the case 70-235-82 with stainless steel collar.

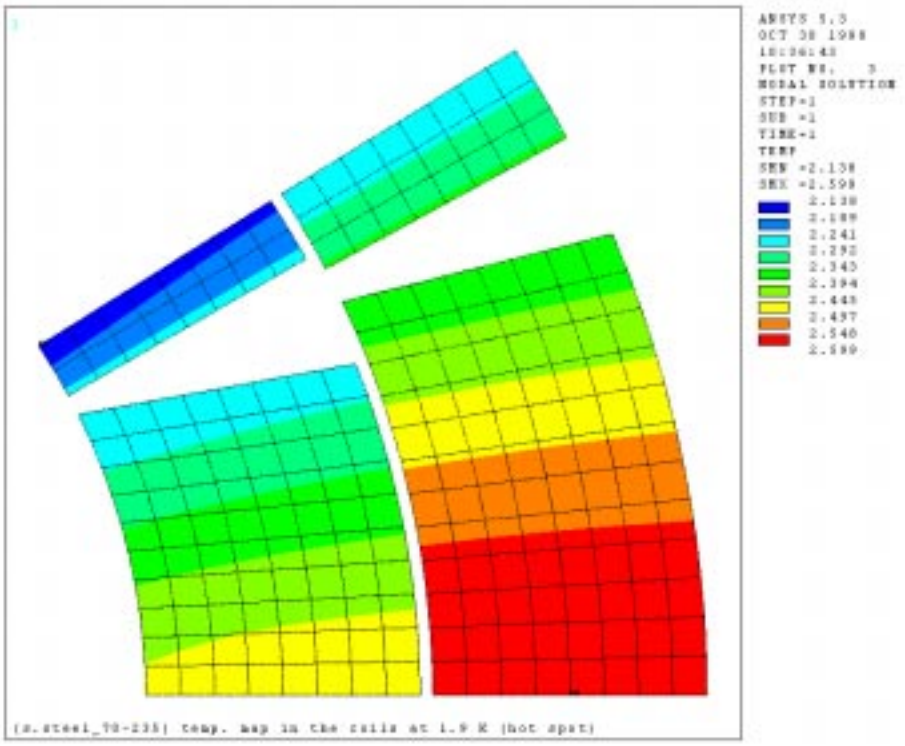

FIG.20: Temperature distribution in the coils for the case 70-235-82 with stainless steel collar.

In Fig. 21 the thermal flux in the whole section is shown while in Fig. 22 is reported the flux toward He_2 crossing the aperture at r = 35 mm.

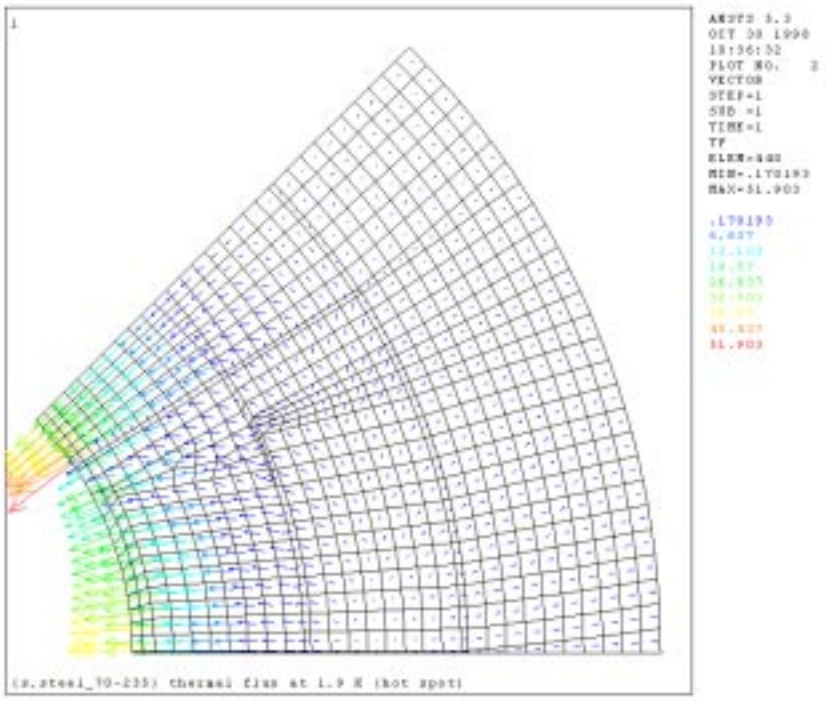

FIG. 21: Thermal flux (W/m^2) for the case 70-235-82 with stainless steel collar.

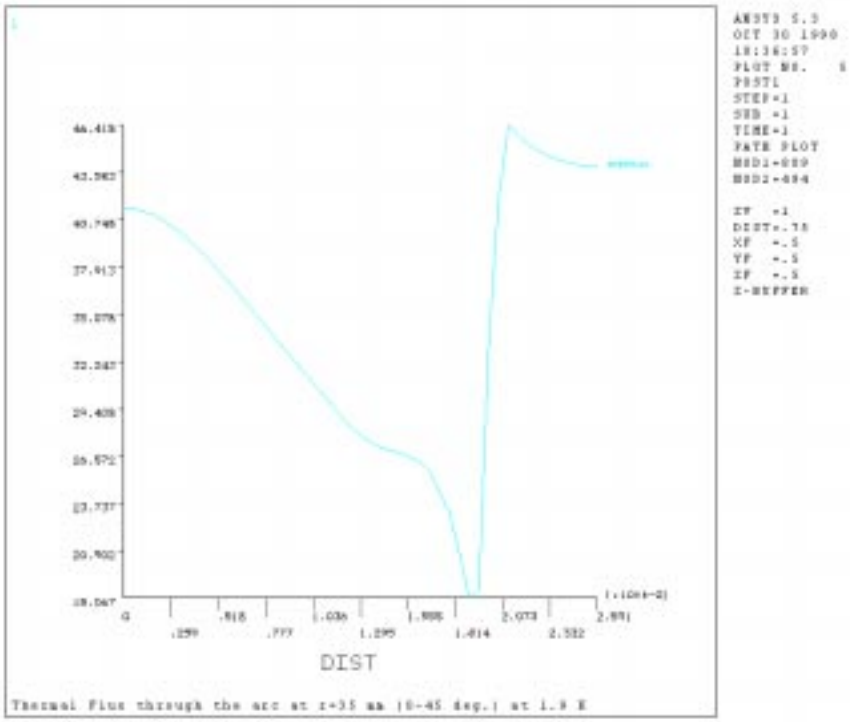

FIG. 22: Thermal flux (W/m^2) through the aperture.

It can be noted that:

- The maximum temperature in the coil is 2.6 K. This is a great increment respect to the helium temperature but, occurring in the outer shell, it has no significant influence on the design.
- The inner shell shows a temperature increment of 0.2 K near the pole, in the peak field region, and an increase of 0.6 K on the mid-plane. Being the field on the mid-plane lower than the peak field of more than 2 tesla, the critical point remains the region where the peak field occurs.
- The heat flow to the helium on the inner aperture has a maximum of 46 W/m^2, generating a temperature gap at the interface of 0.05 K.
- The maximum temperature is not dominated by the heat transfer to fluid but is determined by the heat conduction through the insulation (the temperature drop through the inner ground insulation on the mid-plane is 0.55 K) and by the heat conduction through the collars.

The temperature distributions in the coils in all the other cases at 1.9 K, with stainless steel collars are shown in Figures 23 and 24.

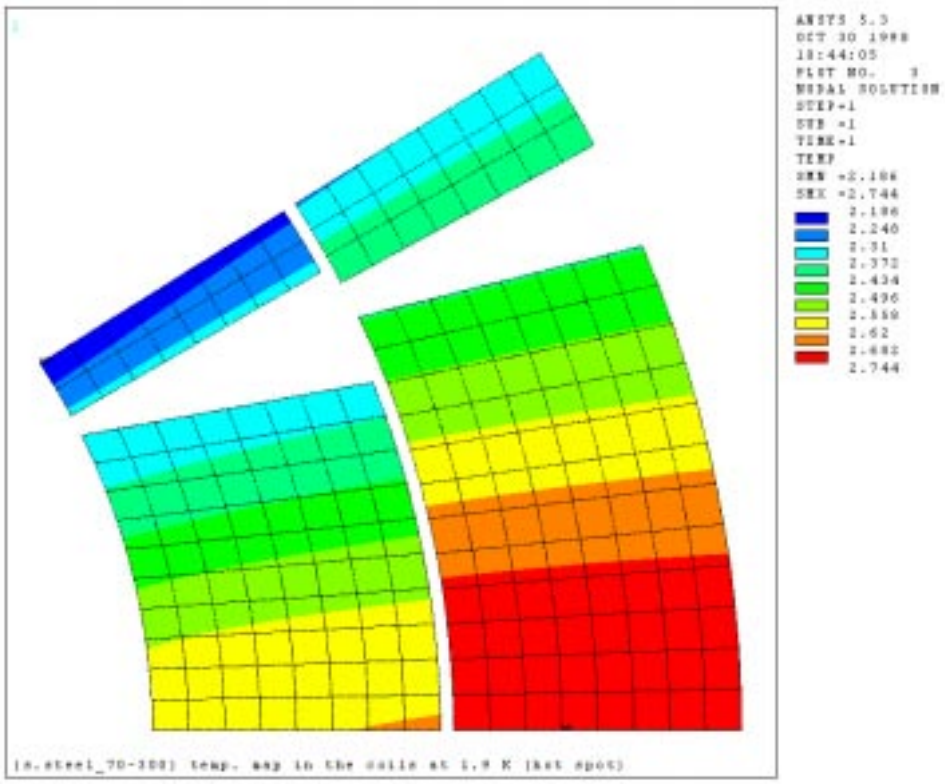

FIG. 23: Temperature distribution in the coils for the case 70-300-105 with stainless steel collar.

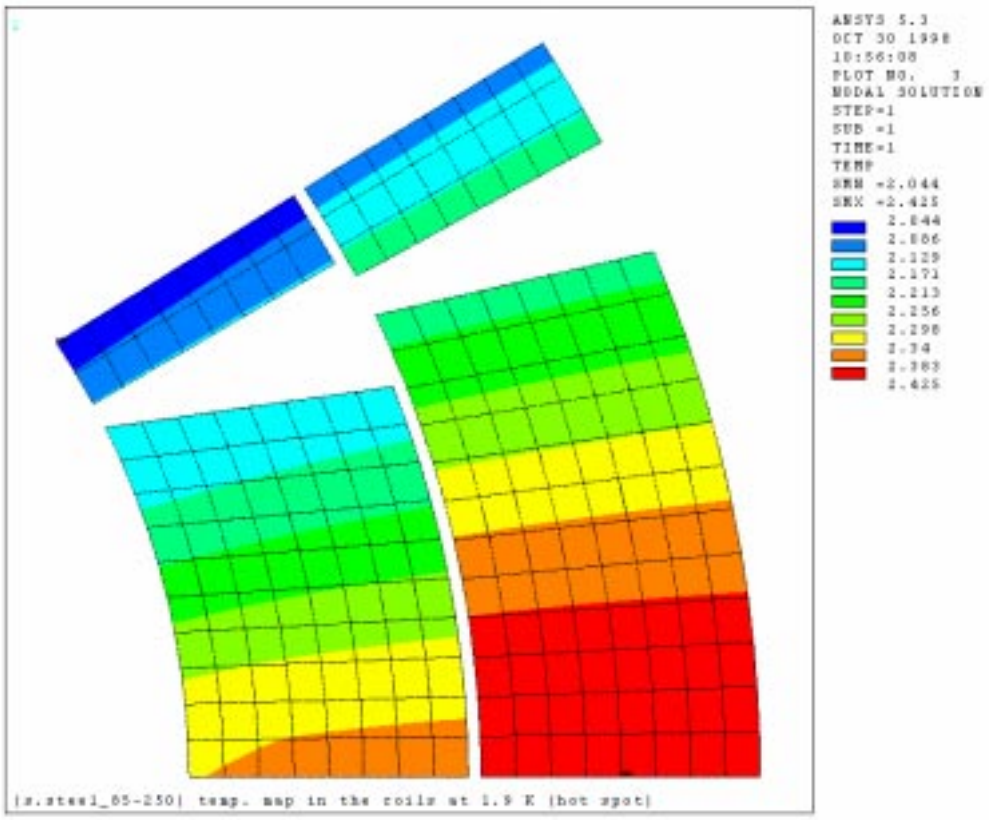

FIG. 24: Temperature distribution in the coils for the case 85-235-82 with stainless steel collar.

Figures 25, 26 and 27 are the same as figs. 20, 23 and 24 respectively, obtained with aluminum collar.

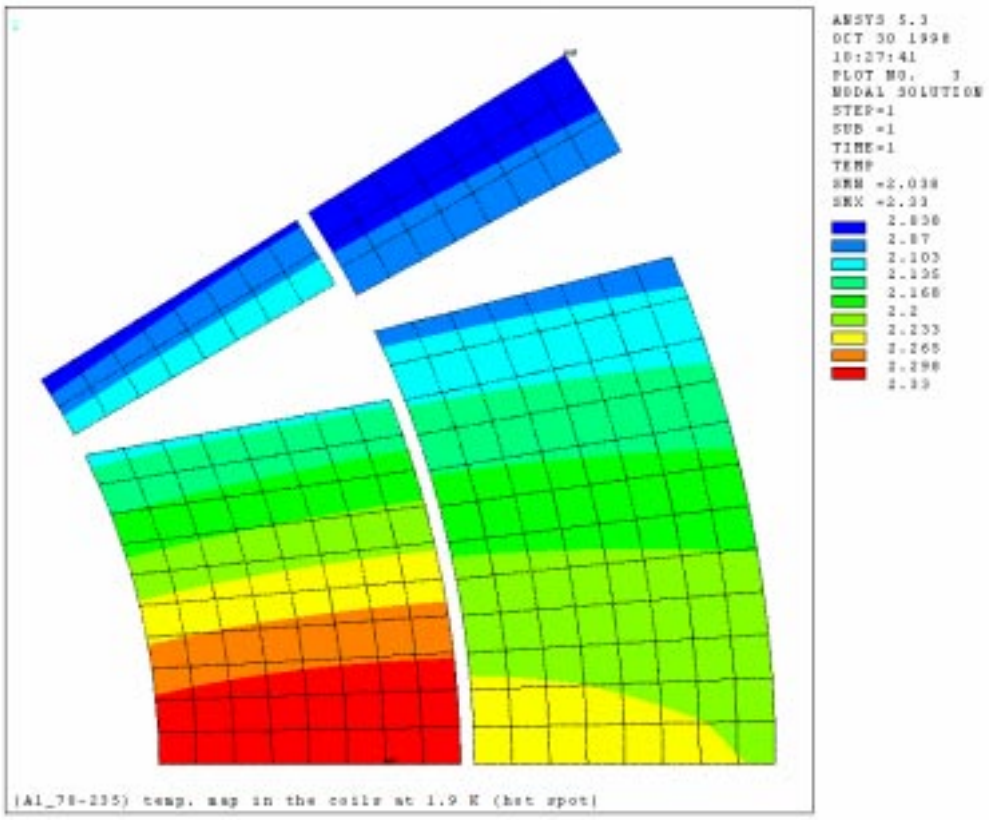

FIG. 25: Temperature distribution in the coils for the case 70-235-82 with aluminum collar.

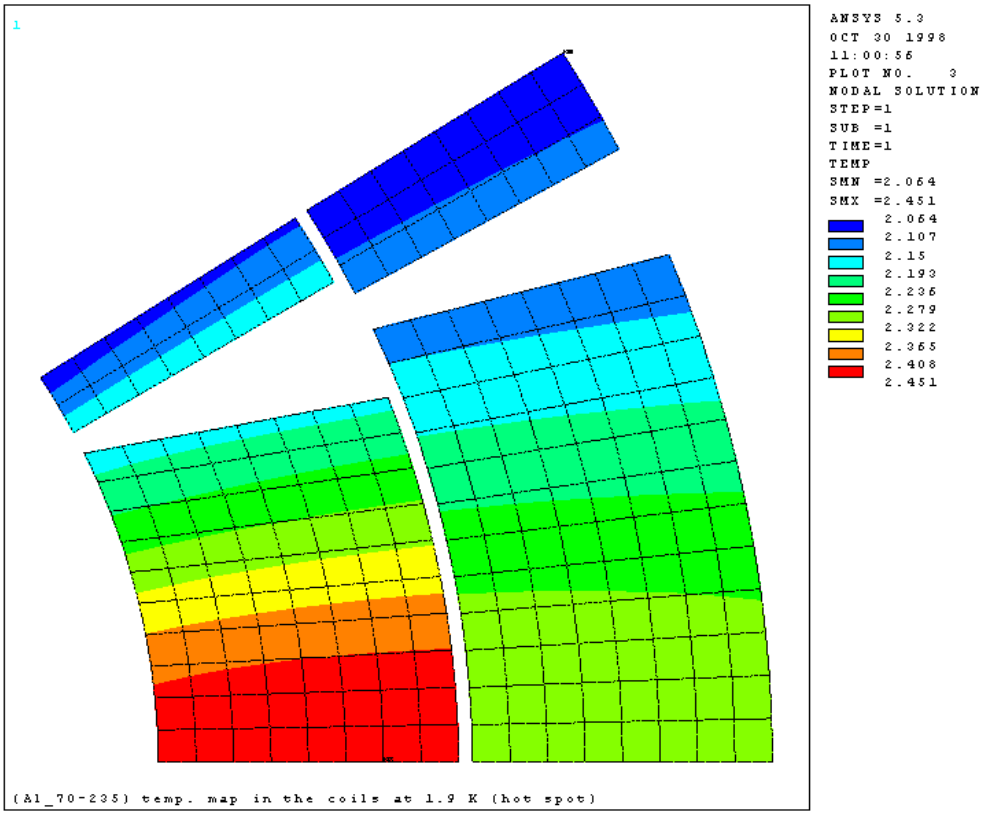

FIG. 26: Temperature distribution in the coils for the case 70-300-105 with aluminum collar.

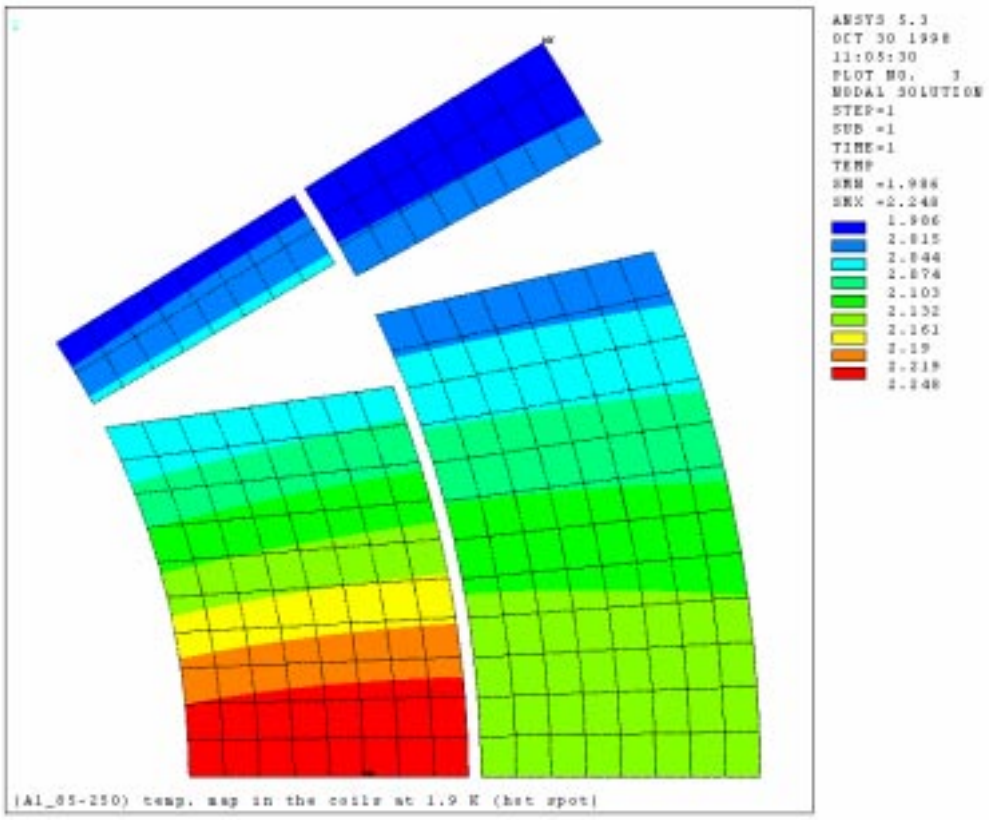

FIG. 27: Temperature distribution in the coils for the case 85-235-82 with aluminum collar.

The effects of the different power and temperature distributions according to quadrupole aperture and gradient, and of using aluminum collars can be seen.

In particular the aluminum, with thermal conductivity higher than stainless steel, more easily removes the power deposed, resulting in a lower temperature increase ad at last in a more safety operating condition. On the contrary the mechanical properties of the stainless steel are better than the aluminum ones, so, for a correct magnet design, a compromise is necessary.

The main results for each design are summarised in Table 8 where in the first part the data already shown in Table 7 are reported again, to ease the reading.

TAB. 8: Total power in the quadrupoles and in the absorbers (in parentheses), peak power density in the inner shell of Q2a for the cases studied (in squared parentheses is the volume of the bins for 85 mm aperture), and thermal results for the cases studied.

Case	**Total power (W)**					**Peak Power in Q2a (mW/cm^3)**			**Thermal Behaviour**				
	Q1	**Q01**	**Q2a**	**Q2b**	**Q3**	**Volume (cm^3)**			**Collar**	**max. Temp. (K)**			**Peak flux**
						12.2 [12.5]	**2.9 [3.13]**	**0.6**	**mat.**	Coil	Layer1	Peak B	W/m^2
1	11.5	8.7	22.4	7.5	17.4	3.2	5.1	7.2	s.steel Al	2.6 2.33	2.45 2.33	2.24 2.11	46 31
2	12.1 (5.6)	6.5 (5.0)	27.5 (11.0)	10.3 (8.5)	14.5 (11.0)	5.7	8.2	9.8	--	--	--	--	--
3	14.4	11.0	25.3	9.5	20.4	4.1	7.5	--	s.steel Al	2.74 2.45	2.6 2.45	2.3 2.15	56 41
4	10.6	8.2	19.4	8.0	6.3	3.8	5.0	--	s.steel Al	2.43 2.25	2.34 2.25	2.12 2.05	33 26
5	13.3 (12.2)	4.5 (4.3)	10.8 (4.9)	7.8 (5.3)	14.6 (10.6)	--	0.3	0.7	--	--	--	--	--

4 STABILITY CONSIDERATIONS

As from the results of the thermal analysis we can state that a sufficient margin stability is achieved in all the cases treated.

As a matter of fact the maximum increase in temperature in the coils occurs in the midplane, where is the maximum energy deposition, but the magnetic filed is not so high to reach a critical working point for the coil. Conversely in the part with highest magnetic field (among the adjacent coils) the temperature increasing is not dangerous for the magnet.

An additional margin can be obtained using aluminum collars, because of the better thermal properties of the aluminum respect to the stainless steel, but the poorer mechanical characteristics of aluminum must be taken into account.

5 CONCLUSIONS

The calculation done show that an acceptable stability margin is available in the reference case.

Variations either on the gradient or on the aperture are not critical for the stability of the magnet, the case with gradient of 300 T/m shows an increase in the power deposed giving less margin stability.

An good fact, from the point of view of the stability of the quadrupoles, is that the maximum of the temperature increase does not coincide with the maximum of the

magnetic field, leaving a larger margin in the operation conditions.

In all the cases considered the power delivered by the reaction products does not require any absorber.

If in different cases, not studied here, the large amount of power delivered to the coils, should be reduced by some absorbers, their effect and dimensioning must be well evaluated, to avoid negative effects, like the ones showed here for the case of uniform cylindrical absorbers.

The use of aluminum collars, respect to the stainless steel ones, is to be preferred for the better thermal characteristics of aluminum, while, on the contrary, stainless steel has better mechanical properties.

Nb_3Sn is, from the point of view of the radiation deposition, a good solution for the second generation of the low β inner triplet, either for increasing the gradient or the aperture.

APPENDIX I - THE BINNING GEOMETRY

Here the different binning geometries for the different aperture are described.

The binning geometry is a tool of FLUKA allowing to store the energy deposition in a geometric structure superimposed to the physical geometry and independent on it. For our convenience a cartesian geometry has been chosen, so the bins are rectangular parallelepipeds with square base. Both the cases of geometries, the 70 mm aperture and the 85 mm one, has been investigated with different dimensions of the bins in order to get the beast resolution to insulate the peak of the energy deposition in the coils. The different binning geometries will be indicated as “medium”, “fine” and, “very fine” geometry, the dimensions and details will be shown in the following. The dimensions of the bins was chosen in order to get the best resolution for the most interesting part of the magnets, without intercepting, when possible, the beam pipe and the coil in the same bin, especially on the median plane where the maximum peak power deposition occurs.

In the following figures the transverse geometry of the quadrupoles, up to the second shell of the coils is shown. The outern part, collar and yoke are not shown.

The radii of the collar and of the yoke are 86.4 mm and 260 mm respectively for the aperture of 70 mm; 93.9 mm and 270 mm are respectively the radii of the collar and of the yoke for aperture of 85 mm.

6.1 Aperture 70 mm

The case with 70 mm aperture has been studied with the medium, the fine and the very fine binning geometry.

6.1.1 Medium binning geometry

In this case the dimensions of the bins is 0.493 x 0.493 x 50 mm^3 for a volume of 12.17 mm^3. The transverse section of the bins superimposed to the cross section of the quadrupoles is shown in Fig.28

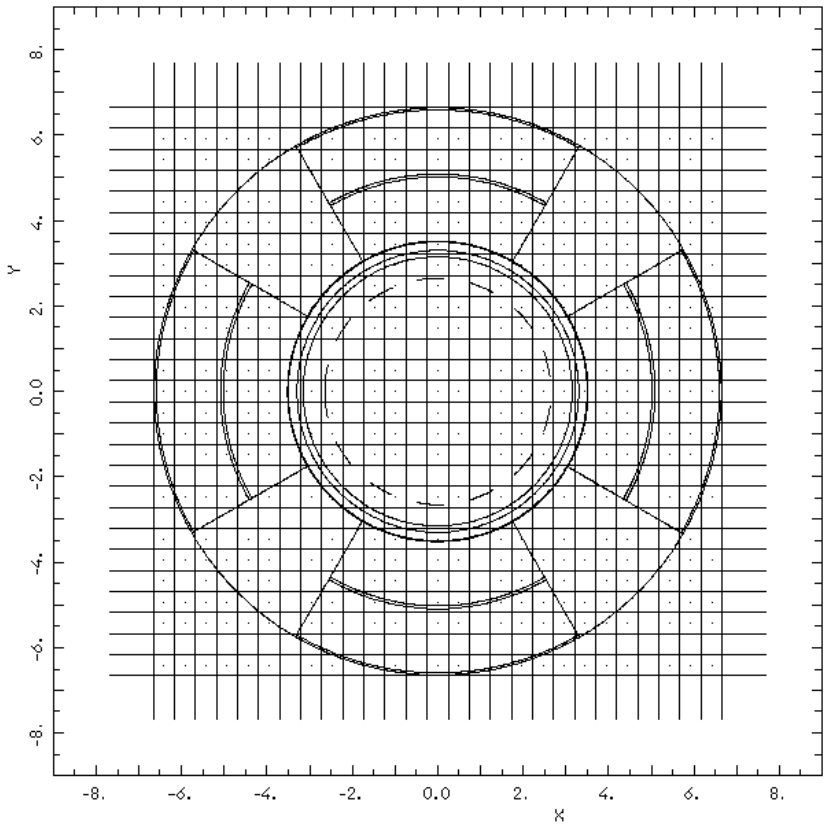

FIG. 28: The medium binning geometry. The dotted line shows the profile of the uniform cylindrical absorber, when considered.

6.1.2 Fine binning geometry

In this case the dimensions of the bins is 0.242 x 0.242 x 50 mm^3 for a volume of 2.93 mm^3. The transverse section of the bins superimposed to the cross section of the quadrupoles is shown in Fig.29.

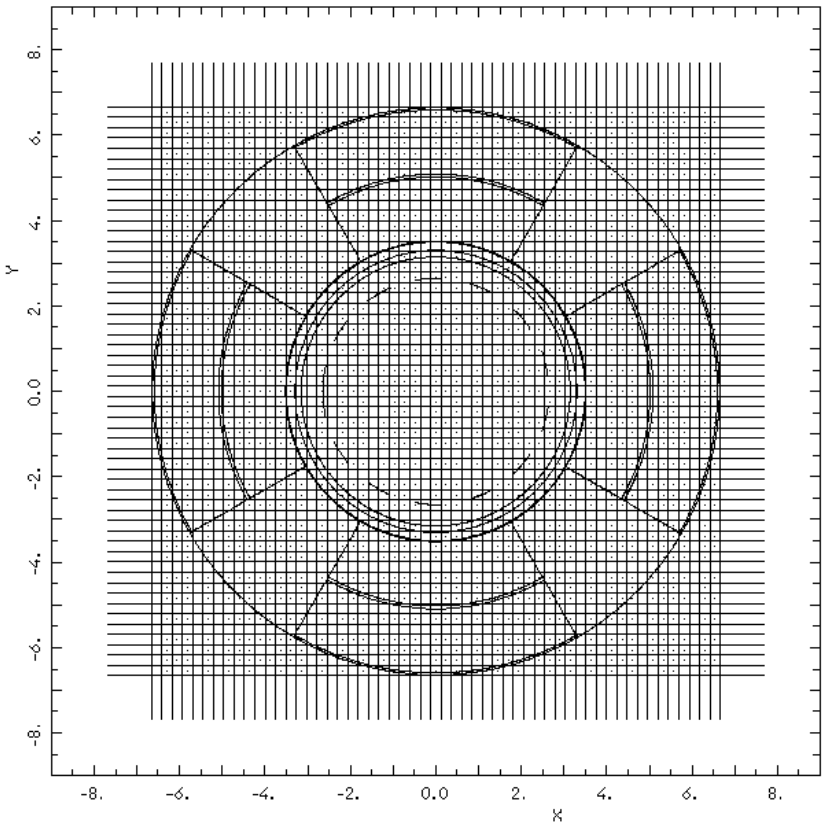

FIG. 29: The fine binning geometry. As in the previous figure the dotted lines shows the profile of the uniform cylindrical absorber.

6.1.3 Very fine binning geometry

In this case the transverse dimensions of the bins are the same as the fine geometry described in the previous sections but the length is reduced to 10 cm, so the dimensions of the bins are 0.242 x 0.242 x 10 mm^3 for a volume of 0.6 mm^3.

6.2 Aperture 85 mm

The case with 85 mm aperture has been studied only with the medium, and the fine geometry.

6.2.1 Medium binning geometry

In this case the dimensions of the bins is 0.5 x 0.5 x 50 mm^3 for a volume of 12.5 mm^3. The transverse section of the bins superimposed to the cross section of the quadrupoles is shown in Fig.30.

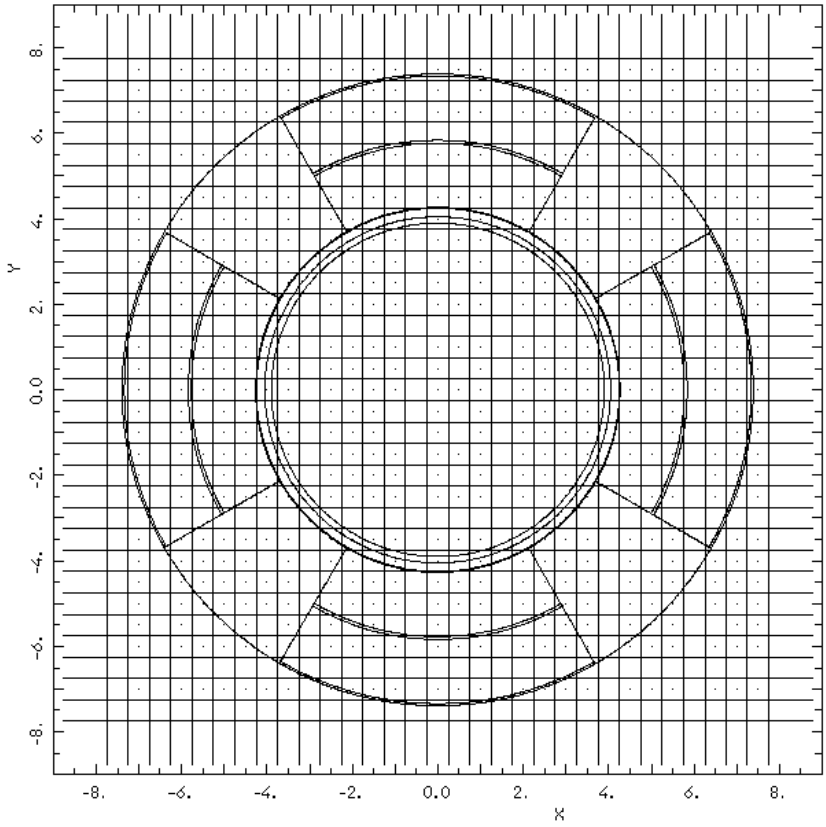

FIG. 30: The medium binning geometry for 85 mm aperture.

6.2.2 Fine binning geometry

In this case the dimensions of the bins is 0.25 x 0.25 x 50 mm^3 for a volume of 3.125 mm^3. The transverse section of the bins superimposed to the cross section of the quadrupoles is shown in Fig. 31.

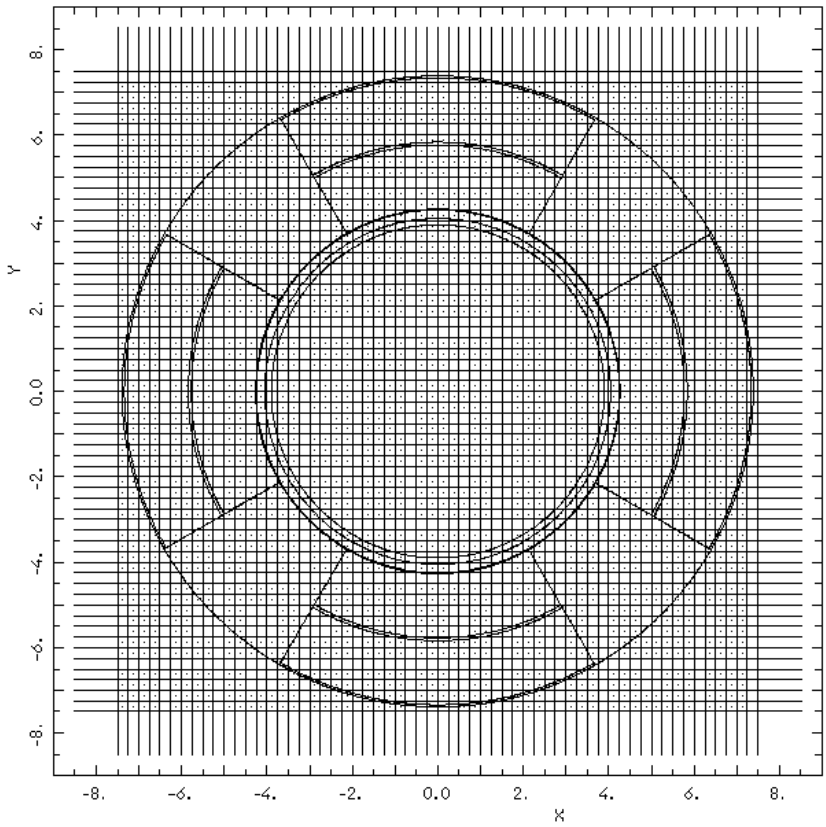

FIG. 31: The fine binning geometry for 85 mm aperture.

APPENDIX II – DTUJET GENERATED PARTICLES

In Tab. 9 the particles generated by DTUJET in the 7+7 TeV “head-on” collision, the particle identification number for FLUKA together with the total energy carried is shown.

TAB. 9: Particles generated by DTUJET

Particle (FLUKA N°)	N° of particles generated by DTUJET	Total Energy(GeV)
p (1)	3680	$3.57332\ 10^{6}$
$\bar{p}$ (2)	2318	$1.75365\ 10^{5}$
e^- (3)	31	$1.10254\ 10^{3}$
e^+ (4)	31	$1.58737\ 10^{3}$
ν (5)	0	0
$\bar{\nu}$ (6)	0	0
γ (7)	6869	$3.78775\ 10^{5}$
n (8)	3304	$1.94866\ 10^{6}$
$\bar{n}$ (9)	2325	$1.69671\ 10^{5}$
μ^+ (10)	0	0
μ^- (11)	0	0
K^0_L (12)	4420	$4.15180\ 10^{5}$
π^+ (13)	38542	$3.41749\ 10^{6}$
π^- (14)	37485	$2.63201\ 10^{6}$
K^+ (15)	4713	$5.25469\ 10^{6}$
K^- (16)	4561	$4.36268\ 10^{5}$
Λ (17)	698	$3.46290\ 10^{5}$
$\bar{\Lambda}$ (18)	584	$5.43050\ 10^{4}$
K^0_S (19)	4471	$3.98703\ 10^{5}$
Σ^- (20)	181	$4.57138\ 10^{4}$
Σ^+ (21)	177	$8.05121\ 10^{5}$
Σ^0 (22)	201	$9.56817\ 10^{5}$
π^0 (23)	43667	$3.39830\ 10^{6}$
K^0 (24)	0	0
$\bar{K}^0$ (25)	0	0
ν_μ (27)	0	0
$\bar{\nu}_\mu$ (28)	0	0
$\bar{\Sigma}^-$ (31)	138	$1.57706\ 10^{4}$
$\bar{\Sigma}^0$ (32)	156	$1.47383\ 10^{4}$
$\bar{\Sigma}^+$ (33)	157	$1.62593\ 10^{4}$
Ξ^0 (34)	59	$1.70057\ 10^{4}$
$\bar{\Xi}^0$ (35)	40	$2.94897\ 10^{3}$
Ξ^- (36)	65	$8.84705\ 10^{3}$
$\bar{\Xi}^+$ (37)	49	$9.03819\ 10^{3}$
Ω (38)	1	2.90109
$\bar{\Omega}$ (39)	2	$3.26078\ 10^{1}$
Charmed (40)	96	$1.99752\ 10^{4}$
TOTAL	159201	$18.2\ 10^{6}$

As we can see the most important particles (the particles carrying most of the energy) are the p,π^+,π^0,$\pi^-$and n. The energy carried by these particles is 1.5 x 10^7 GeV corresponding to the 82 % of the total energy realized.

Considering the K^+, K^-, K^0_L , γ and Λ the carried energy is 1.7 x 10^7 corresponding to the 93 % of the total.

The particle realized in the interaction have a very wide spectrum in energy and momentum as we can see in Fig.32 - 36.

In Fig. 32 and 33 the transverse momentum of the 3680 protons generated by DTUJET is shown.

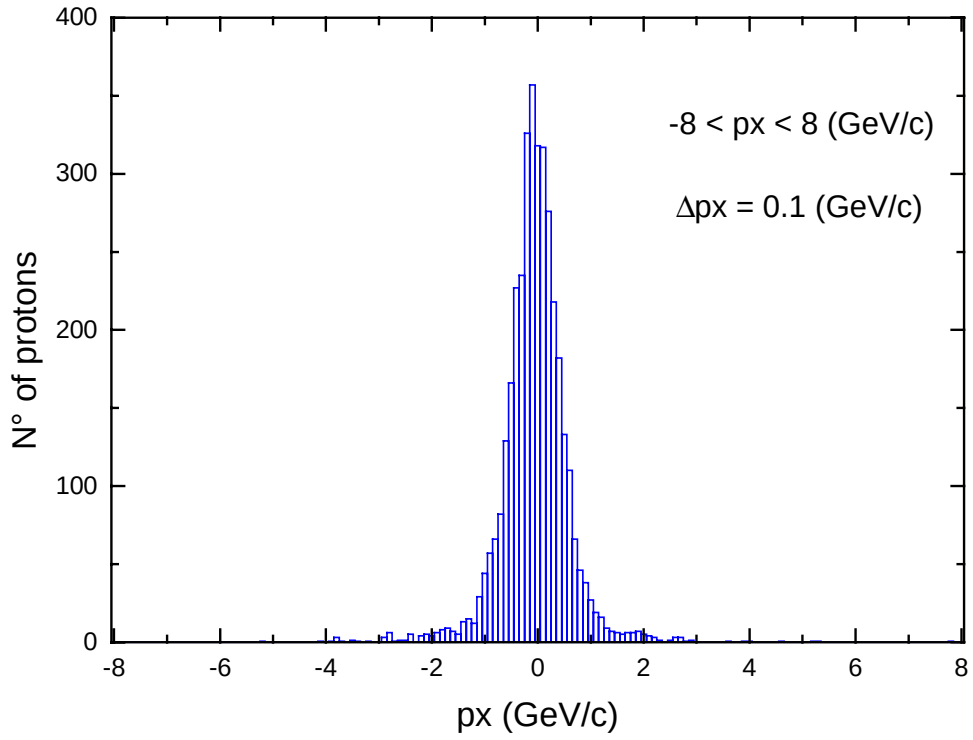

FIG. 32: Horizontal momentum distribution of the protons, as from DTUJET

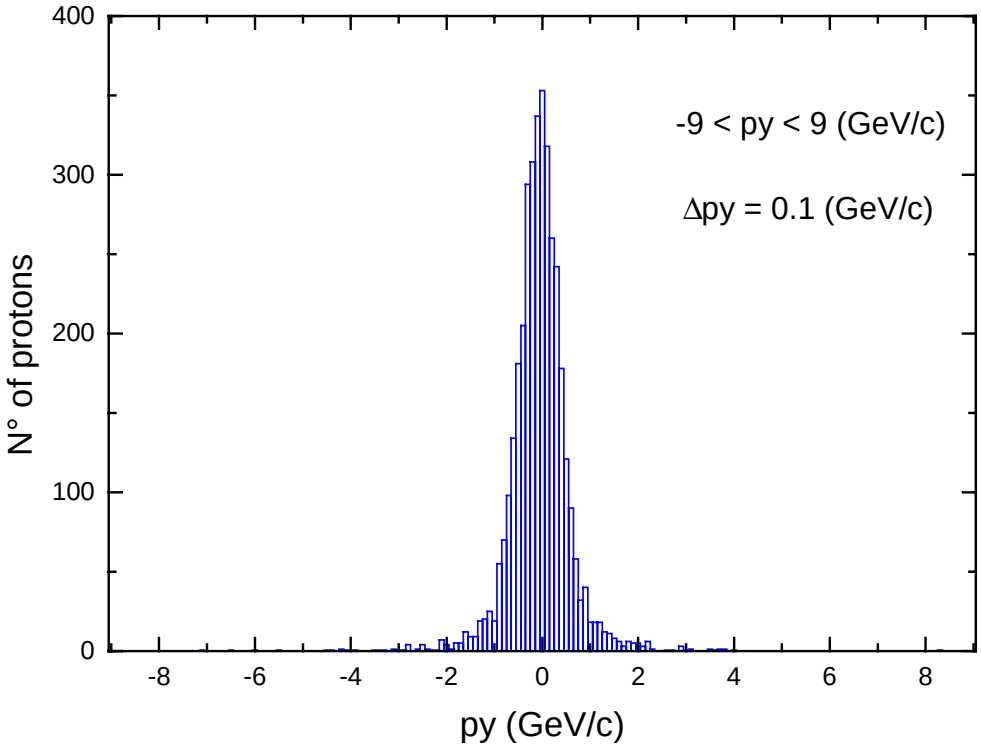

FIG. 33: Proton vertical momentum distribution as from DTUJET

In Fig. 34 and 35 the longitudinal and the total momentum of the protons is shown.

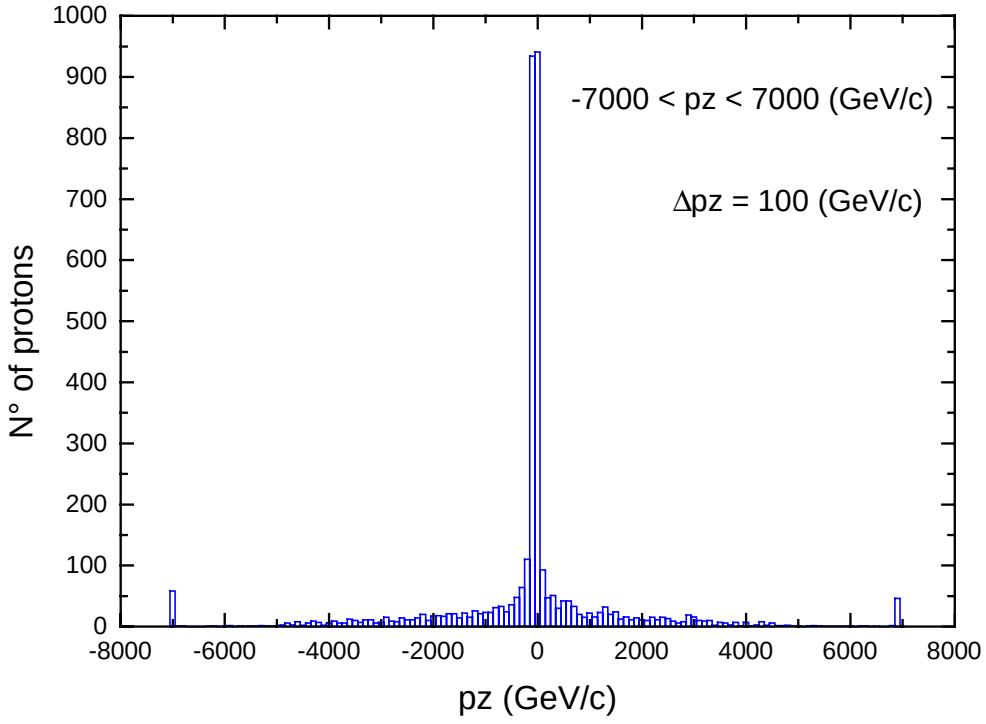

FIG. 34: Longitudinal momentum distribution for the protons, as from DTUJET

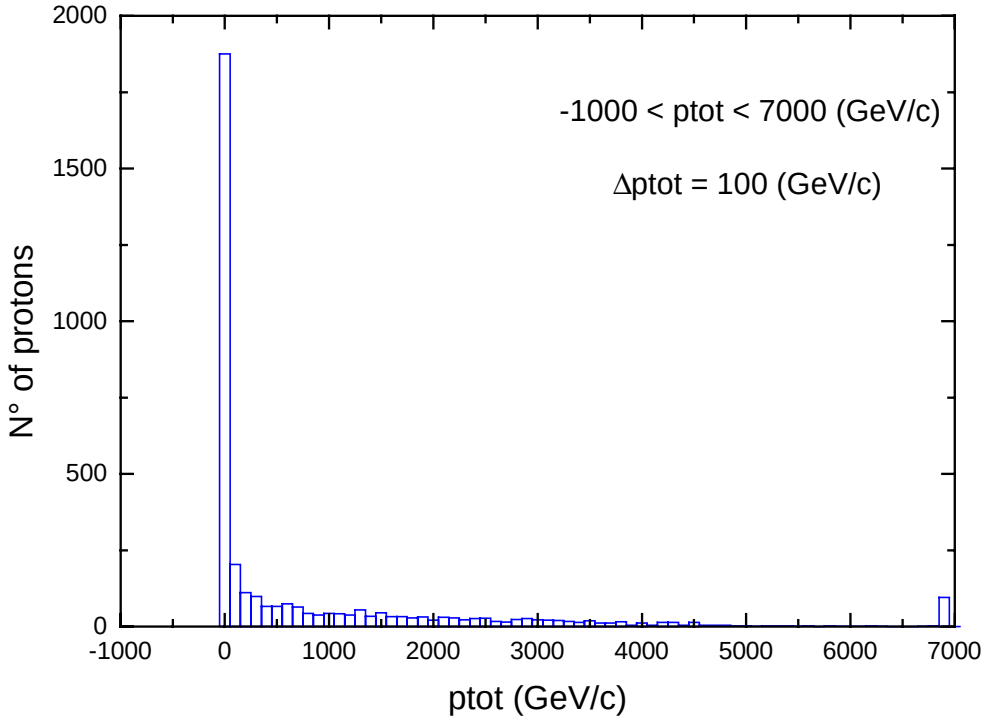

FIG. 35: Proton total momentum distribution as from DTUJET

In Fig 36 the total energy distribution is shown. The peak at the edge of the distributions represents the protons of the single diffractive events.

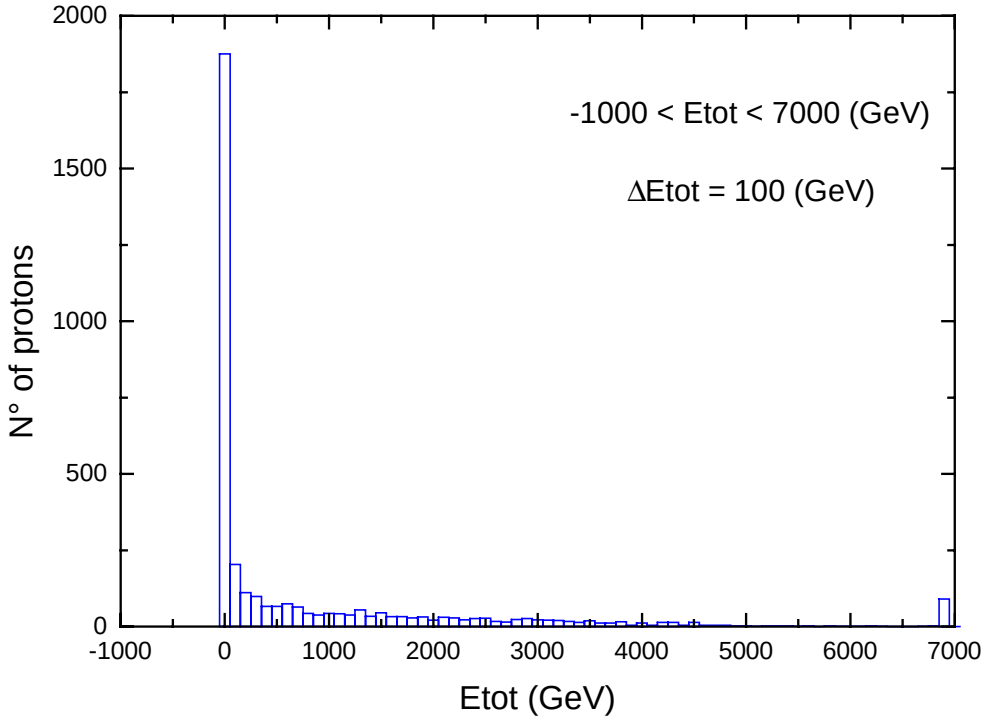

FIG. 36: Total energy distribution for protons, as from DTUJET

In Fig. 37 the distribution of the magnetic rigidity Bρ is shown.

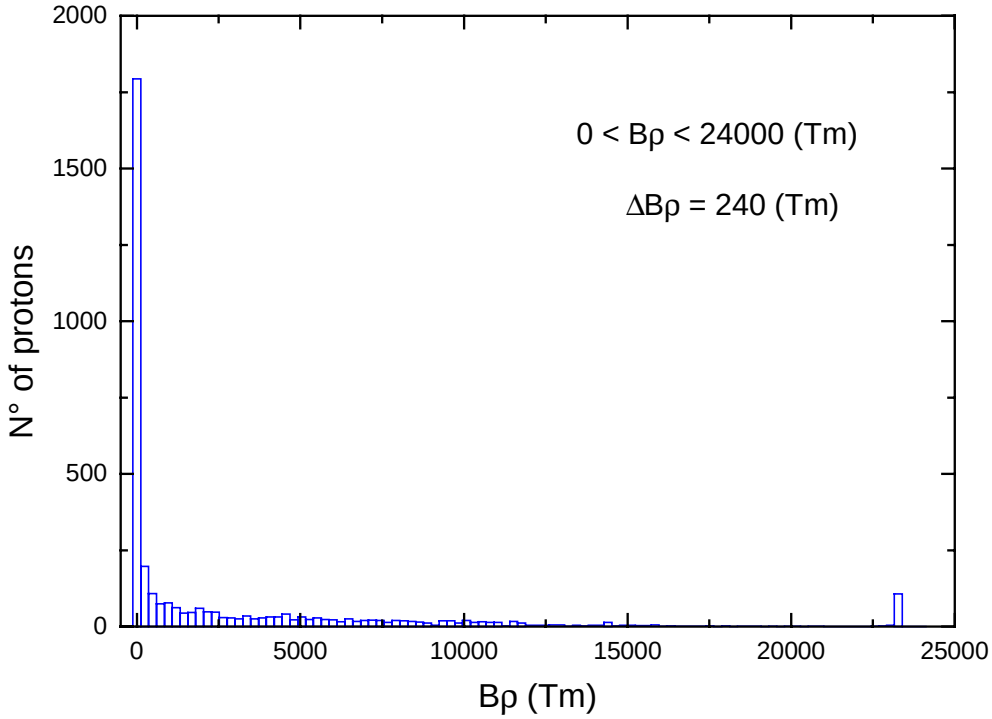

FIG. 37: Magnetic rigidity of the protons as from DTUJET

The distributions in the figs. 32 - 36 show a very wide spectrum in momentum and energy, and consequently in Bρ, so the protons (and all the reaction products) cannot be treated as a beam so they must be tracked singularly.

6 APPENDIX III – TRACKING OUTPUT

Here the results of the tracking for the reference case of 235 T/m main gradient, 70 mm aperture and 82 T/m are shown. In Table 10 the number of the particles that hit the elements are shown. The identification number of the particle is the same as in table 9 or in the following Table 11, while the identification number of the elements is the same of Table 1; for more clarity the quadrupole magnets (element 4,8,12,and 16) are indicated with bolded character in order to point out them.

Let's recall that only the charged particles are tracked in the magnetic structure of the insertion, while the neutral particles are processed by FLUKA at their generation, i.e. at the Interaction Point.

TAB. 10: Particles hitting the various beam line elements for the reference case.

	Element of the beam line															
	1	2	3	**4**	5	6	7	**8**	9	10	11	**12**	13	14	15	**16**
1	2192	293	0	73	14	83	22	78	5	3	4	100	4	3	35	95
2	2188	87	0	13	1	5	3	6	0	0	2	6	0	0	1	2
3	27	2	0	1	0	1	0	0	0	0	0	0	0	0	0	0
4	28	2	0	0	0	0	0	0	0	0	0	0	0	0	0	1
5	0	0	0	0	0	0	0	0	0	0	0	0	0	0	0	0
6	0	0	0	0	0	0	0	0	0	0	0	0	0	0	0	0
7	0	0	0	0	0	0	0	0	0	0	0	0	0	0	0	0
8	0	0	0	0	0	0	0	0	0	0	0	0	0	0	0	0
9	0	0	0	0	0	0	0	0	0	0	0	0	0	0	0	0
10	0	0	0	0	0	0	0	0	0	0	0	0	0	0	0	0
11	0	0	0	0	0	0	0	0	0	0	0	0	0	0	0	0
12	0	0	0	0	0	0	0	0	0	0	0	0	0	0	0	0
13	35126	1431	0	599	50	219	84	253	14	11	13	248	20	4	58	113
14	34858	1268	0	427	38	164	59	172	20	10	9	158	14	4	28	57
15	4352	185	0	40	3	26	5	27	3	0	4	17	4	0	6	10
16	4258	187	0	41	6	16	8	14	1	0	1	7	0	0	6	8
17	0	0	0	0	0	0	0	0	0	0	0	0	0	0	0	0
18	0	0	0	0	0	0	0	0	0	0	0	0	0	0	0	0
19	0	0	0	0	0	0	0	0	0	0	0	0	0	0	0	0
20	73	6	0	0	0	1	0	0	0	0	0	3	1	0	0	1
21	135	10	0	4	2	3	1	3	0	0	0	2	1	1	1	1
22	0	0	0	0	0	0	0	0	0	0	0	0	0	0	0	0
23	0	0	0	0	0	0	0	0	0	0	0	0	0	0	0	0
24	0	0	0	0	0	0	0	0	0	0	0	0	0	0	0	0
25	0	0	0	0	0	0	0	0	0	0	0	0	0	0	0	0
26	0	0	0	0	0	0	0	0	0	0	0	0	0	0	0	0
27	0	0	0	0	0	0	0	0	0	0	0	0	0	0	0	0
28	0	0	0	0	0	0	0	0	0	0	0	0	0	0	0	0
29	0	0	0	0	0	0	0	0	0	0	0	0	0	0	0	0

30	0	0	0	0	0	0	0	0	0	0	0	0	0	0	0	0
31	59	0	0	0	0	0	0	1	0	0	0	1	0	0	0	1
32	0	0	0	0	0	0	0	0	0	0	0	0	0	0	0	0
33	150	4	0	0	0	0	0	1	0	0	0	1	0	0	0	1
34	0	0	0	0	0	0	0	0	0	0	0	0	0	0	0	0
35	0	0	0	0	0	0	0	0	0	0	0	0	0	0	0	0
36	32	0	0	0	0	0	0	0	0	0	0	0	0	0	0	1
37	22	2	0	0	0	0	0	0	0	0	0	0	0	0	0	0
38	0	0	0	0	0	0	0	0	0	0	0	0	0	0	0	0
39	0	0	0	0	0	0	0	0	0	0	0	0	0	0	0	0
40	0	0	0	0	0	0	0	0	0	0	0	0	0	0	0	0

In the following table is shown the total number of the particles that hits the beam pipe or decay in flight or escape forward from the inner triplet.

TAB. 11: Particles hitting the beam pipe, decaying or escaping the system for the reference case.

Particle (FLUKA N°)	Particles hitting the beam pipe	Particles escaping	Particles decaying	Total
p (1)	3004	676	0	3680
$\bar{p}$ (2)	2314	4	0	2318
e^- (3)	31	0	0	31
e^+ (4)	31	0	0	31
ν (5)	0	0	0	0
ν^- (6)	0	0	0	0
g (7)	0	0	0	0
n (8)	0	0	0	0
$\bar{n}$ (9)	0	0	0	0
μ^+ (10)	0	0	0	0
μ^- (11)	0	0	0	0
K_L^0 (12)	0	0	0	0
π^+ (13)	38243	299	0	38542
π^- (14)	37286	198	1	37485
K^+ (15)	4682	31	0	4713
K^- (16)	4553	8	0	4561
Λ (17)	0	0	0	0
$\bar{\Lambda}$ (18)	0	0	0	0
K_S^0 (19)	0	0	0	0
Σ^- (20)	85	5	91	181
Σ^+ (21)	164	13	0	177
Σ^0 (22)	0	0	0	0
π^0 (23)	0	0	0	0
K^0 (24)	0	0	0	0
$\bar{K}^0$ (25)	0	0	0	0
ν_μ (27)	0	0	0	0
$\bar{\nu}_\mu$ (28)	0	0	0	0
$\bar{\Sigma}^-$ (31)	62	0	76	138
$\bar{\Sigma}^0$ (32)	0	0	0	0
$\bar{\Sigma}^+$ (33)	157	0	0	157
Ξ^0 (34)	0	0	0	0
$\bar{\Xi}^0$ (35)	0	0	0	0
Ξ^- (36)	33	1	31	65
Ξ^+ (37)	24	1	24	49
Ω (38)	0	0	1	1
$\bar{\Omega}$ (39)	0	0	2	2
Charmed (40)	0	0	0	0

In table 12 the total energy in GeV of the charged particles that hit the beam pipe under the quadrupole the is shown.

TAB. 12: Charged particles hitting the beam pipe under the quadrupole.

Particle (FLUKA N°)	**Q 1**	**Q01**	**Q2a**	**Q2b**	**Q3**
p (1)	3.9632E+04	8.5090E+04	8.0149E+04	1.2705E+05	1.7076E+05
$\bar{p}$ (2)	4.9675E+03	3.7995E+03	5.1789E+03	6.5053E+03	3.6761E+03
e^- (3)	3.0022E+02	3.5598E+02	0.0000E+00	0.0000E+00	0.0000E+00
e^+ (4)	0.0000E+00	0.0000E+00	0.0000E+00	0.0000E+00	8.8620E+02
ν (5)	0.0000E+00	0.0000E+00	0.0000E+00	0.0000E+00	0.0000E+00
ν^- (6)	0.0000E+00	0.0000E+00	0.0000E+00	0.0000E+00	0.0000E+00
g (7)	0.0000E+00	0.0000E+00	0.0000E+00	0.0000E+00	0.0000E+00
n (8)	0.0000E+00	0.0000E+00	0.0000E+00	0.0000E+00	0.0000E+00
$\bar{n}$ (9)	0.0000E+00	0.0000E+00	0.0000E+00	0.0000E+00	0.0000E+00
μ^+ (10)	0.0000E+00	0.0000E+00	0.0000E+00	0.0000E+00	0.0000E+00
μ^- (11)	0.0000E+00	0.0000E+00	0.0000E+00	0.0000E+00	0.0000E+00
K_L^0 (12)	0.0000E+00	0.0000E+00	0.0000E+00	0.0000E+00	0.0000E+00
π^+ (13)	2.0955E+05	1.4690E+05	1.9265E+05	2.5957E+05	1.8766E+05
π^- (14)	1.4058E+05	1.1527E+05	1.2593E+05	1.6217E+05	8.8684E+04
K^+ (15)	1.8090E+04	2.0929E+04	2.9074E+04	1.8712E+04	1.7855E+04
K^- (16)	1.3916E+04	1.2560E+04	1.3324E+04	8.0474E+03	1.6917E+04
Λ (17)	0.0000E+00	0.0000E+00	0.0000E+00	0.0000E+00	0.0000E+00
$\bar{\Lambda}$ (18)	0.0000E+00	0.0000E+00	0.0000E+00	0.0000E+00	0.0000E+00
K_S^0 (19)	0.0000E+00	0.0000E+00	0.0000E+00	0.0000E+00	0.0000E+00
Σ^- (20)	0.0000E+00	9.7918E+02	0.0000E+00	3.8055E+03	1.9283E+03
Σ^+ (21)	1.3818E+03	2.4757E+03	3.7127E+03	1.8705E+03	1.5814E+03
Σ^0 (22)	0.0000E+00	0.0000E+00	0.0000E+00	0.0000E+00	0.0000E+00
π^0 (23)	0.0000E+00	0.0000E+00	0.0000E+00	0.0000E+00	0.0000E+00
K^0 (24)	0.0000E+00	0.0000E+00	0.0000E+00	0.0000E+00	0.0000E+00
$\bar{K}^0$ (25)	0.0000E+00	0.0000E+00	0.0000E+00	0.0000E+00	0.0000E+00
ν_μ (27)	0.0000E+00	0.0000E+00	0.0000E+00	0.0000E+00	0.0000E+00
$\bar{\nu}_\mu$ (28)	0.0000E+00	0.0000E+00	0.0000E+00	0.0000E+00	0.0000E+00
$\bar{\Sigma}^-$ (31)	0.0000E+00	0.0000E+00	1.6130E+03	1.2538E+03	1.6330E+03
$\bar{\Sigma}^0$ (32)	0.0000E+00	0.0000E+00	0.0000E+00	0.0000E+00	0.0000E+00
$\bar{\Sigma}^+$ (33)	0.0000E+00	0.0000E+00	8.2668E+02	1.0839E+03	1.9603E+03
Ξ^0 (34)	0.0000E+00	0.0000E+00	0.0000E+00	0.0000E+00	0.0000E+00
$\bar{\Xi}^0$ (35)	0.0000E+00	0.0000E+00	0.0000E+00	0.0000E+00	0.0000E+00

Ξ^-	(36)	0.0000E+00	0.0000E+00	0.0000E+00	0.0000E+00	1.5313E+03
Ξ^+	(37)	0.0000E+00	0.0000E+00	0.0000E+00	0.0000E+00	0.0000E+00
Ω	(38)	0.0000E+00	0.0000E+00	0.0000E+00	0.0000E+00	0.0000E+00
$\overline{\Omega}$	(39)	0.0000E+00	0.0000E+00	0.0000E+00	0.0000E+00	0.0000E+00
Charmed	(40)	0.0000E+00	0.0000E+00	0.0000E+00	0.0000E+00	0.0000E+00
TOTAL ENERGY (GeV)		**4.2841E+05**	**3.8836E+05**	**4.5245E+05**	**5.9006E+05**	**4.9507E+05**
TOTAL POWER (W)		**21.1**	**19.1**	**22.3**	**29.1**	**24.4**

Here, at first sight, it seems that the quadrupole with the highest power deposition is Q2b, but let's recall that this is the energy, or power, delivered at the beam pipe under the quadrupole by the charged particles only. By taking into account of the neutral particles and the treatment of the interaction with the quadrupole materials by FLUKA we will get the values reported in the paper.

In table 13 the values of the total energy released at the beam pipe under the quadrupole, the total energy of the decaying and of the forward escaping are summarised (again, for the charged particles only).

TAB. 13: Total energy of the particles hitting the beam pipe, decaying or escaping the system.

	Hitting the beam pipe	**Escaping**	**Decaying**	**Total**
Energy (GeV)	6.74610E+06	4.17921E+06	1.34621E+04	1.09388E+07
Power (W)	332.26	205.83	0.66	538.75

9 REFERENCES

(1) "LHC Conceptual Design", Tech. Rep., CERN, October 1995, CERN/AC/95-05.

(2) R.Ostojic et al., "Quench Performance and Field Quality Measurements of the First LHC Low-β Quadrupole Model", Particle Accelerator Conference,**42**, N°3, (1997).

(3) R.Ostojic et al., "Design and Construction of a One-Meter Model for the 70 mm Aperture Quadrupole for the LHC low-β Insertions", Proc. of MT13, 1750, Vancouver B.C., (1993).

(4) A.Yamamoto et al., "Development of a Superconducting Insertion Quadrupole Model Magnet for the Large Hadron Collider", 15th Magnet Technology, Beijing, (1997).

(5) Y.Ajimo et al. "Development and Test Results of a low-β Quadrupole Model for the LHC", VI European Particle Accelerator Conference, Stockholm, (1998).

(6) G.Sabbi et al."Magnetic Design of a High Gradient Quadrupole for the LHC low-β Insertions", Particle Accelerator Conf., **42**, N°3, (1997).

(7) A.den Ouden et.al, "Application of Nb_3Sn Superconductors in High Field Magnets", IEEE Trans on Appl.Supercon., **7**, N°2, (1997).

(8) S.Caspi et al.,"Development of High Field Dipole Magnets for Future Accelerators", 15th Magnet Technology, Beijing, (1997).

(9) A.Morsh, "Local Power Distribution from Particle Losses in the LHC inner Triplet Magnet Q1", CERN AT/94-06 (DI), LHC Note 265.

(10) P.Aurenche et al. "DTUJET-93", Computer Physics Comm., **83**, 107,(1994).

(11) "ATLAS Technical Design Report" - 7; CERN/LHCC 97-19.

(12) A. Fassò et al. "FLUKA: Present Status and Future Development", IV Int.Conf. On Calorimetry in HEP, 493, (1994).

(13) G.Ambrosio et al. "Magnetic Field, Multipole Expansion and Peak Field in 2D for Superconducting Accelerator Magnets" I.N.F.N. Report. I.N.F.N./TC-96/15, October 2nd 1996.

(14) N.Kimura et al. "Heat Transfer Characteristics of Rutherford-Type Superconducting Cables in Pressurized He II", Applied Superconductivity Conference, Palm Desert (1998).